Design and Transient Performance Analysis of a Functionally Graded Rotor for High-Speed Synchronous Reluctance Motors in Electric Vehicle

By

JAVKHLAN Bulgan

B2200292

A Bachelor Thesis

Submitted to Faculty of Mechanical and Electrical Engineering

In fulfillment of the requirements for the degree of

Mechanical Engineering

Of the German-Mongolian institute for Resources and Technology

Supervisor 1/ Examiner 1: Prof.Dr. Sungchil Lee

Supervisor 2/ Examiner 2: Prof.Dr. Kim Young Suk

Ulaanbaatar/ Nalaikh

2026

Table of Contents

Table of Contents 2
Acknowledgement 5
Abstract 6
List of Abbreviations 7
List of Tables 8
List of Figures 8
1. Introduction 10
1.1 Background of Electric Vehicle Propulsion Systems 10
1.2 Synchronous Reluctance Motors (SynRM) 11
1.3 Conflict between mechanical strength and magnetic efficiency 12
1.4 Functionally graded materials (FGMs) 13
1.5 Research Objectives 14
2. Literature Review 15
2.1 Principles of Reluctance Torque 15
2.1.1 Introduction to Reluctance Torque 15
2.1.2 The Saliency Ratio 16
2.1.3 Impact on Power Density 16
2.2 Additive Manufacturing in Electrical Machines 17
2.2.1 Contextual Motivation 18
2.2.2 Overview of AM Processes Used in Electrical Machines 18
2.2.3 Applications in Motor Components 18
2.2.4 Functionally Graded Structures 18
2.2.5 Performance Improvements Reported in Literature 19
2.2.6 Current Limitations 19
2.3 Review of non-magnetic fillers 20
2.4 Magnetic Saturation and Iron Losses 21
3. Design and Methodology 22
3.1 Electromagnetic Geometry Optimization: 24-slot stator vs. 4-pole rotor design parameters. 22
3.1.1 Rotor Pole Parameters and Flux Barriers 23

3.2 Winding Strategy 23
3.2.1 Advantages of the Double-Layer Configuration 24
3.3 Rotor Topology Design 24
3.3.1 The Geometric Foundation of Saliency 24
3.3.2 Optimizing Barrier Shape and Curvature 25
3.3.3 The Rib-to-Barrier Insulation Ratio 25
3.3.4 Managing Structural Integrity with Multi-Barrier Layouts 25
3.4 Finite Element Method Magnetics (FEMM) Setup 25
3.4.1 Boundary Conditions and Domain Definition 26
3.4.2 Mesh Refinement and Discretization 26
3.4.3 Circuit Definitions and Phase Mapping 26
3.4.4 Material Property Assignment 26
4. Simulation and Performance Analysis 27
4.1 Comparative Analysis of Rotor Architectures 27
4.2 Flux Density Distribution 31
4.2.1 Overview 31
4.2.2 A Solid Rotor Case 31
4.2.3 Standard Rotor with Bridges 31
4.2.4 Rotor without Bridges 32
4.3 Torque and Power Characterization 32
4.3.1 Torque Calculation 32
4.3.2 Motor Excitation and Target Torque 32
4.3.3 Torque Comparison Across Rotor Cases 33
4.4 Saliency Ratio Evaluation 33
4.4.1 Solid Rotor 34
4.4.2 With Bridges 34
4.4.3 Without Bridges 35
4.5 Summary 35
5. Mechanical and Structural Validation 36
5.1 Centrifugal Stress Analysis 36
5.1.1 Simulation Setup 36

5.1.2 CASE A: FGM ROTOR 36
5.1.3 CASE B Standard Rotor 38
5.1.4 Comparative Analysis 39
5.1.5 Discussion 40
5.2 FGM Interface Bond Strength 40
5.2.1 Material System Overview 40
5.2.2 Nature of FGM Interface 41
5.2.3 Bond Strength in 3D Printed FGM Fabrications 42
5.2.4 Effective Properties at the Interface Zone 43
5.2.5 Interface Integrity Under Centrifugal Loading 43
5.3 Thermal Management: Heat dissipation in high-current density windings 44
5.3.1 Overview 44
5.3.2 Winding Configuration and Current Density 44
5.3.3 Copper Loss Calculation 45
5.3.4 Heat Generation Distribution 46
5.3.5 Cooling Strategy 46
5.3.6 Thermal Relevance to FGM Rotor 47
6. Conclusion and Future Recommendations 48
6.1 Summary of Findings: Magnetic flux 48
6.1.1 Overview 48
6.1.2 Flux Leakage in Standard Bridges Rotor 48
6.1.3 Flux Leakage Elimination in FGM Rotor 48
6.1.4 Effect on Saliency and Torque Capability 49
6.2 Contributions to Resource Technology: Reducing reliance on rare-earth magnets. 50
6.3 Future Work: Experimental prototyping and multi-material 3D printing calibration 50
7. References 52
Statutory Declaration 53
Student's Declaration of Academic Integrity & AI Transparency 54

Acknowledgement

I would like to express my sincere gratitude to my first supervisor, Prof. Dr. Sungchil Lee, for his guidance and support throughout this thesis. His expertise in mechanical engineering was particularly valuable in shaping the structural and mechanical aspects of this work, including the rotor layer analysis and centrifugal stress validation. His constructive feedback and encouragement at every stage helped me navigate the more challenging parts of this research.

I am also deeply grateful to my second supervisor, Prof. Dr. Young Suk Kim, for his technical advice and continuous support on the electromagnetic side of this thesis. His recommendation to use FEMM software for electromagnetic simulation proved to be a key decision in this work. FEMM provided the simulation environment needed to analyze and compare the three rotor configurations, and the results obtained from it form the core of the electromagnetic analysis presented here.

Special thanks go to my peer Enkhjin, who generously helped me with the ANSYS structural analysis. His assistance during the simulation process was essential, especially given the computational challenges encountered during the structural validation work.

I would also like to thank my peer Bumbayar, who supported me greatly throughout the entire thesis process. His help, encouragement, and presence made this journey significantly easier and more enjoyable.

Finally, I am grateful to the German-Mongolian Institute for Resources and Technology for providing the academic environment and resources that made this research possible.

Abstract

This thesis presents the design and performance analysis of a functionally graded (FG) rotor for a high-speed Synchronous Reluctance Motor (SynRM) targeting 150 kW at 18,000 RPM for electric vehicle applications. The core problem addressed is the conflict between mechanical strength and magnetic efficiency in high-speed SynRM rotors, where steel bridges provide structural support but cause q-axis flux leakage that reduces torque production.

A functionally graded material system using M-19 silicon steel and phosphor bronze is proposed to replace steel bridges. Three rotor configurations were compared: a solid baseline rotor, a standard bridged rotor, and a bridgeless FGM rotor with phosphor bronze barrier fill. The rotor geometry was designed in Autodesk Inventor Professional as individual lamination profiles. Electromagnetic simulation was performed using FEMM 4.2 in the magnetostatic regime, where a 24-slot 4-pole motor was excited with balanced three-phase peak currents of I_A = 300 A, I_B = I_C = −150 A. Flux linkage, phase inductance, and Maxwell stress tensor torque were extracted from the circuit properties panel for each rotor case. Structural analysis was conducted in ANSYS Static Structural 2026 R1 on individual lamination layers under a rotational body load of 18,000 RPM, with the shaft bore face fixed as the boundary condition. Full rotor stack simulation was not possible due to computational hardware limitations.

Electromagnetic results show the FGM rotor reduces q-axis flux leakage by 7.3% and improves the saliency indicator by 58% compared to the standard bridged design. Structural results show the standard steel rotor reaches 289.86 MPa at the barrier ribs with a safety factor of only 1.24, while the FGM rotor reduces peak strain by 58.4% and raises the safety factor to 1.79. Peak copper loss is calculated at 4.08 kW, requiring water jacket cooling. The phosphor bronze fill also improves rotor thermal conductivity from 23 to 50 W/mK.

The proposed design uses no rare-earth materials, presenting a sustainable and cost-effective alternative for high-speed EV traction motors and contributing to the development of domestic electric vehicle engineering capability in Mongolia.

List of Abbreviations

AM — Additive Manufacturing

ANSYS — Analysis System (FEA Software)

BMS — Battery Management System

B-H — Magnetic Flux Density — Magnetic Field Strength Curve

CTE — Coefficient of Thermal Expansion

DED — Direct Energy Deposition

FDM — Fused Deposition Modeling

FEA — Finite Element Analysis

FEMM — Finite Element Method Magnetics

FGM — Functionally Graded Material

FP — Fully Pitched

GaN — Gallium Nitride

HIP — Hot Isostatic Pressing

ICE — Internal Combustion Engine

IM — Induction Motor

IPM — Interior Permanent Magnet

LFP — Lithium Iron Phosphate

LPBF — Laser Powder Bed Fusion

MMF — Magnetomotive Force

MTPA — Maximum Torque Per Ampere

PA-CF — Polyamide Carbon Fiber

PMSM — Permanent Magnet Synchronous Motor

SiC — Silicon Carbide

SLM — Selective Laser Melting

SLS — Selective Laser Sintering

SMC — Soft Magnetic Composite

SoC — State of Charge

SPM — Surface-Mounted Permanent Magnet

SynRM — Synchronous Reluctance Motor

THD — Total Harmonic Distortion

List of Tables

#	Caption	Location
Table 2.1	Comparison of non-magnetic filler materials	§2.3
Table 4.1	All Phase Inductances (Flux/Current from FEMM)	§4.4
Table 5.1	Key Results (FGM vs Standard Rotor structural comparison)	§5.1.4
Table 5.1	Key Material Properties (M-19 Silicon Steel vs Phosphor Bronze)	§5.2.1
Table 6.1	Inductance Results (Solid / Standard / FGM rotor comparison)	§6.1

List of Figures

#	Caption	Location
Figure 1.1	SynRM real example	§1.2
Figure 1.2	Bridges of the Rotor	§1.3
Figure 2.1	Reluctance torque	§2.1.1
Figure 3.1	Comparison of Concentrated winding and Distributed winding	§3.2
Figure 4.1	Case A: Solid Rotor Base Case	§4.1
Figure 4.2	Case B: Standard Steel Bridge Design	§4.1
Figure 4.3	Case C: FGM Flux Barriers	§4.1
Figure 5.1	Strain Result FGM Rotor	§5.1.2
Figure 5.2	Stress Result FGM Rotor	§5.1.2
Figure 5.3	Stress Result Standard Rotor	§5.1.3
Figure 5.4	Strain Result Standard Rotor	§5.1.3
Figure 5.5	Slot Area	§5.3

List Of Equations

#	Caption	Location
Equation 1.2.1	Electromagnetic Torque	§1.2
Equation 2.1.2.1	Saliency Ratio	§2.1.2
Equation 2.1.2.2	Reluctance torque	§2.1.2
Equation 2.1.3.1	Stator Current Magnitude	§2.1.3
Equation 2.1.3.2	Total Electromagnetic Torque	§2.1.3
Equation 2.4.1	Electrical Frequency	§2.4
Equation 4.3.1.1	Total Electromagnetic Torque	§4.3.1
Equation 4.3.2.1	Torque	§4.3.2
Equation 5.1.2.1	Yield Strain	§5.1.2
Equation 5.2.2.1	Volume Fraction of Filler material	§5.2.2
Equation 5.3.2.1	Cross-sectional Area of one Conductor	§5.3.2
Equation 5.3.2.2	Current Density	§5.3.2
Equation 5.3.3.1	Resistive Copper Loss	§5.3.3
Equation 5.3.3.2	Resistance of One Conductor	§5.3.3
Equation 5.3.3.3	Copper Loss per slot at Peak Current	§5.3.3
Equation 5.3.4.1	Electrical Frequency	§5.3.4
Equation 5.3.5.1	Temperature Rise	§5.3.5

1. Introduction

1.1 Background of Electric Vehicle Propulsion Systems

Electric vehicles (EV) are getting a lot of attention nowadays. There are many reasons to have an EV, zero emission, low maintenance and torque. Since its only power source is battery there are no emissions. EV has a simpler design than internal combustion cars which reduces maintenance.

The development of EVs dates back to the late 19th century. However, their adoption remained limited due to the dominance of gasoline-powered vehicles, low battery efficiency, and lack of supporting infrastructure. In recent decades, advancements in battery technologies, particularly lithium-ion batteries, have dramatically improved energy density, charging speed, and driving range, making EVs more practical and commercially viable.

A modern EV propulsion system is a closed-loop power flow consisting of four primary modules. 1) The Energy Storage System, 2) the Power Inverter, 3) the Electric Motor, 4) the Transmission.

1. Most modern systems utilize Lithium-ion or Lithium Iron Phosphate (LFP) battery packs. These act as the DC (Direct Current) reservoir for the vehicle. The Battery Management System (BMS) acts as the brain, monitoring cell voltage, temperature, and State of Charge (SoC).
2. Since batteries provide DC but most high-efficiency motors require AC (Alternating Current), the inverter is the critical middleman. It uses high-speed switching transistors, increasingly Silicon Carbide (SiC) or Gallium Nitride (GaN) for better thermal efficiency, to convert DC into a variable-frequency AC signal. This allows for precise control over the motor's speed and torque.
3. There are 3 most dominant types of the motors used in propulsion. Permanent Magnet Synchronous Motors (PMSM), Induction Motors (IM), Synchronous Reluctance Motors (SynRM). This thesis focused on the rotor of SynRms.
4. Unlike ICE vehicles that need multi-speed gearboxes to stay in a narrow power band, electric motors produce 100% of their peak torque at 0 RPM. This allows most EVs to use a single-speed reduction gear, simplifying the drivetrain and reducing mechanical losses.

The industry is currently pivoting toward 800V architectures (up from the standard 400V) to allow for faster charging and thinner, lighter wiring. Additionally, research into axial flux motors (which look like flat pancakes rather than long cylinders) promises even higher torque density for performance-oriented applications.

1.2 Synchronous Reluctance Motors (SynRM)

Synchronous Reluctance Motors (SynRM) are a class of AC electric machines that produce torque through the principle of magnetic reluctance variation. Unlike induction motors or permanent magnet synchronous motors, SynRMs do not rely on rotor windings or permanent magnets. Instead, torque is generated due to the tendency of magnetic flux to follow the path of least reluctance within the rotor structure.

The rotor of a SynRM is typically constructed with flux barriers that create anisotropic magnetic properties, resulting in different inductances along the direct axis (d-axis) and quadrature axis (q-axis). This difference in inductance is essential for torque production. When a rotating magnetic field is produced by the stator windings, the rotor aligns itself with the magnetic field in such a way that minimizes magnetic reluctance, thereby generating torque.

The electromagnetic torque in a SynRM is primarily dependent on the difference between the d-axis and q-axis inductances. This relationship can be expressed as:

$$T_e = \frac{3}{2} p(L_d - L_q) i_d i_q$$

Equation 1.2.1 Electromagnetic Torque

T_e *=electromagnetic torque*

p*=number of pole pairs*

L_q, L_d *= d-axis and q-axis inductances*

i_d , i_q *= d-axis and q-axis currents*

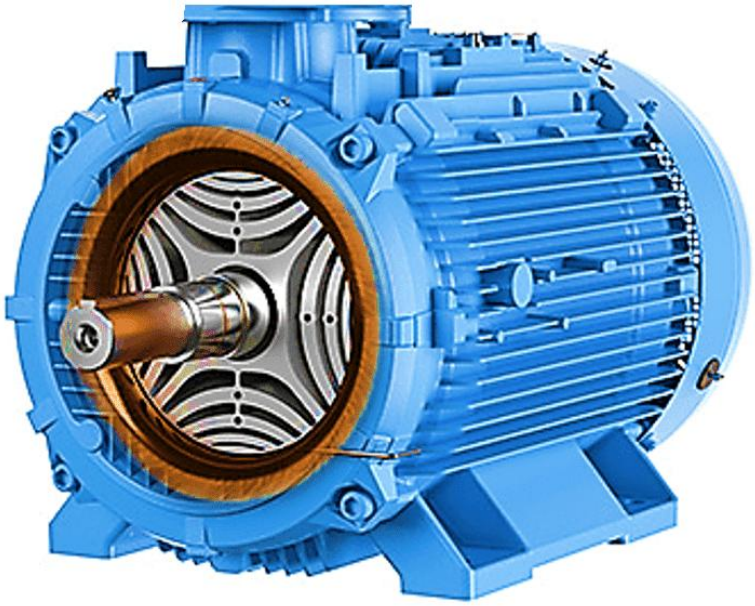


Figure 1.1 SynRm real example

One of the key advantages of SynRMs is their simple and robust rotor construction, which usually consists of laminated steel with strategically designed flux barriers. The absence of rotor windings eliminates copper losses in the rotor, while the lack of permanent magnets reduces dependency on rare-earth materials, lowering cost and improving sustainability.

1.3 Conflict between mechanical strength and magnetic efficiency

To achieve high torque, the rotor needs a high magnetic saliency ratio, the difference between the ease of flux flow in one direction versus another. As speeds increase, the centrifugal forces act to tear the rotor apart, forcing engineers into a difficult design corner.

At high angular velocities, the rotor laminations are subjected to extreme centrifugal stress. In a SynRM or IPM rotor, the "ribs" or bridges (the thin sections of steel at the outer edge and between flux barriers, shown in fig1.2) are the only components holding the rotor segments together.

From an electromagnetic standpoint, these bridges are a liability. Silicon steel is highly permeable, meaning magnetic flux prefers to travel through it rather than across the air-filled flux barriers. When bridges are thick, they provide a "short circuit" for the magnetic

flux. Instead of crossing the air gap to interact with the stator and produce torque, the flux "leaks" through the bridges within the rotor itself.



Figure 1.2 Bridges of the Rotor

As the difference between L_d and L_q shrinks the power factor worsen.

1.4 Functionally graded materials (FGMs)

The development of high-performance engineering structures operating under extreme thermal, mechanical, and chemical conditions has exposed the fundamental limitations of conventional homogeneous and laminated composite materials. This has provided the primary motivation for the investigation and adoption of functionally graded materials (FGMs) as a superior alternative in demanding structural applications.

Functionally graded material (FGM) belongs to a class of advanced composite materials that is characterized by variation in composition, microstructure, as well as properties across the dimension of the material. [3]

One of the primary motivations for using FGMs in SynRM rotor design is the improvement of **mechanical integrity under high-speed operation**. As rotor speed increases, centrifugal forces cause significant stress, particularly near the outer regions of the rotor. By grading the material properties—such as increasing strength or stiffness toward the outer radius—FGMs can reduce stress concentrations and enhance structural durability, thereby preventing mechanical failure.

Another important motivation is **enhanced electromagnetic performance**. In SynRM rotors, torque production depends on the difference in magnetic reluctance along different axes. FGMs enable the spatial tuning of magnetic permeability, which can be used to increase the inductance difference between the d-axis and q-axis. This leads to an improved saliency ratio and higher torque output without increasing motor size.

From a design perspective, FGMs offer **greater flexibility and optimization potential**. Engineers can tailor material distributions to achieve a balance between electromagnetic efficiency, mechanical strength, and thermal performance. This multi-functional optimization is particularly valuable in next-generation EV motors, where compactness and performance are critical.

1.5 Research Objectives

The primary aim of this research is to design, simulate, and optimize a high-speed Synchronous Reluctance Motor (SynRM) rotor utilizing Functionally Graded Materials (FGM) to achieve a peak power output of **150 kW** at a rated speed of **18,000 RPM**.

The first objective is to develop a multi-barrier rotor geometry that maximizes the saliency ratio (ξ) while minimizing torque ripple. This involves using Finite Element Method (FEM) analysis to optimize the placement, curvature, and thickness of the flux-carrying steel ribs. The goal is to ensure that the magnetic field distribution is optimized for a 24-slot stator with distributed windings, targeting a saliency ratio exceeding **5.0**.

A core objective is to replace traditional mechanical steel bridges with non-magnetic FGM fillers. This research will evaluate the electromagnetic impact of substituting air-filled barriers with high-strength, non-magnetic materials (such as PA-CF or Phosphor Bronze). The objective is to quantify the reduction in magnetic flux leakage and the subsequent gain in torque density, aiming for a **10–15%** improvement in peak torque compared to a conventional bridged-rotor design.

The final objective is to benchmark the proposed FGM rotor against a standard solid-bridge SynRM. This comparative study will analyze the motor's efficiency map, thermal behavior, and power-to-weight ratio. The objective is to demonstrate that the FGM approach successfully resolves the "High-Speed Paradox," providing a viable, sustainable, and rare-earth-free alternative for high-performance electric vehicle traction systems.

2. Literature Review

2.1 Principles of Reluctance Torque

2.1.1 Introduction to Reluctance Torque

Reluctance torque is the fundamental operating principle of synchronous reluctance motors (SynRM). It arises from the tendency of magnetic flux to follow the path of least reluctance in a magnetic circuit. In a SynRM, the rotor is intentionally designed with anisotropic magnetic properties, meaning that its magnetic reluctance differs along two orthogonal axes: the direct axis (d-axis) and the quadrature axis (q-axis). When a rotating magnetic field is generated by the stator, the rotor aligns itself such that the magnetic flux flows along the path of minimum reluctance (d-axis). This alignment process produces torque without the need for rotor windings or permanent magnets.The machine torque can be maximized by finding the best insulation ratios, while the torque ripple can be minimized by determining the best rotor slot pitch in the d-axis.[6]

To understand this mechanism properly, consider the electromagnetic torque expression derived from the energy stored in the magnetic field of a two-pole salient-pole machine. In the synchronously rotating d-q reference frame, with the direct axis (d-axis) aligned with the rotor's minimum reluctance path and the quadrature axis (q-axis) leading by 90° electrical.

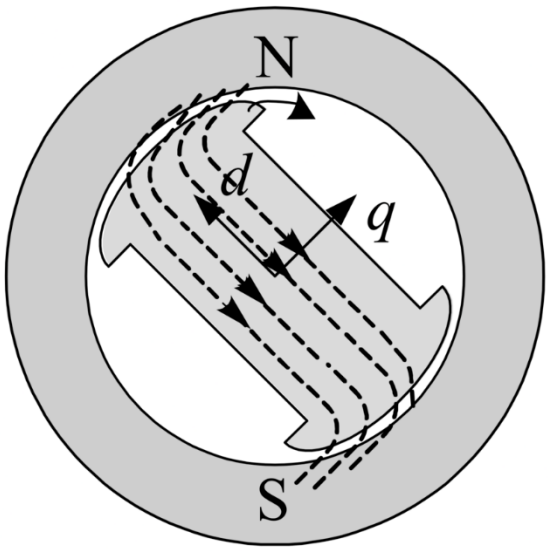


Figure 2.1 Reluctance torque

2.1.2 The Saliency Ratio

The degree of magnetic saliency is quantified by the saliency ratio, defined as:

$$\xi = \frac{L_q}{L_d}$$

Equation 2.1.2.1 Saliency Ratio

The saliency ratio is a comparison of how easily magnetic flux flows through a rotor in two different directions. It measures the high magnetic conductivity of the intended path versus the high resistance of the paths blocked by air gaps or barriers.

A high ratio means the motor can more effectively "grab" and rotate the rotor using magnetic reluctance. This results in higher torque and better efficiency without the need for permanent magnets. Essentially, the greater the contrast between these two paths, the better the motor performs.

In surface-mounted permanent magnet (SPM) machines, the magnets are placed on the rotor surface. Since the permeability of modern rare-earth magnets is close to that of air $\mu_r \approx 1.05$, the effective air gap is magnetically uniform, yielding $L_d \approx L_q$ and ξ≈1. The reluctance torque contribution in such machines is therefore negligible.

In interior permanent magnet (IPM) machines, the magnets are embedded within the rotor laminations. The d-axis flux encounters the high-reluctant magnet material in its path, reducing L_d and L_q. The q-axis flux, by contrast, travels through bridges of iron with comparatively low reluctance, resulting in $L_q > L_d$ and consequently ξ>1. For well-designed IPM rotors, saliency ratios in the range ξ≈2– 4 are typical, while in synchronous reluctance machines (SynRMs), which carry no permanent magnets and rely entirely on reluctance torque — values of ξ ≈ 6–12 or higher are achievable through the use of multiple flux barriers.

It is instructive to rewrite the reluctance torque term to make the role of ξ explicit. With the substitution $L_q = \xi L_d$:

$$T_{rel} = \frac{2}{3} p L_d (1 - \xi) i_d i_q = \frac{2}{3} \mathrm{p L_d} (1 - \xi) \mathrm{i_d\ i_q}$$

Equation 2.1.2.2 Reluctance Torque

2.1.3 Impact on Power Density

The saliency ratio ξ exerts a direct and fundamental influence on the achievable power density of an electrical machine, with implications for both the torque-per-ampere capability and the flux-weakening range the two principal metrics governing the power envelope of a machine drive system.

Torque-per-ampere capability. For a given stator current magnitude

$$\mathrm{I_s} = \sqrt{(\mathrm{i_d^2} + \mathrm{i_q^2})}$$

Equation 2.1.3.1 Stator Current Magnitude

The current angle β (measured from the q-axis) that maximises total torque satisfies the MTPA condition. In the IPM case, the total torque as a function of β is:

$$T_e = \frac{2}{3} p \left[\psi_{pm} I_s \cos\beta + \frac{1}{2} (L_d - L_q) {I_s}^2 \sin 2\beta \right]$$

Equation 2.1.3.2 Total Electromagnetic Torque

As ξ increases, the coefficient of the reluctance term $\frac{1}{2}(\mathrm{L_d} - \mathrm{L_q})\mathrm{I_s^2}$ grows in magnitude, causing the MTPA locus to shift further into negative idi_d id territory. The reluctance torque augments the excitation torque, allowing the machine to produce greater total torque for the same copper loss — a direct improvement in torque density without requiring additional magnet mass. In the limiting case of a pure SynRM ($\Psi_{\mathrm{pm}} = 0$), the optimal current angle approaches β=45°, and the torque is sustained entirely by reluctance.

2.2 Additive Manufacturing in Electrical Machines

The adoption of Additive Manufacturing (AM) in the electrical machine industry represents a shift from "Design for Manufacture" to "Manufacture for Design." While traditional laminations are limited by 2D stamping constraints, 3D printing allows for complex geometries that optimize both thermal and electromagnetic paths.

"The 3D-printed PMSM showed a 48% increase in core loss compared to the target motor. However, the proposed hybrid PMSM reduced the ratio of the electrical steel sheet by more than 25% compared to 3D-printed PMSM. The validity of the proposed model was verified using the finite element method." [1]

2.2.1 Contextual Motivation

Traditional motor manufacturing limits design freedom. Laminations must be stamped, coils must fit through slot openings, and cooling channels must be machinable. These constraints mean most motors share similar geometries shaped more by what is easy to make than by what performs best.

Additive manufacturing (AM) removes many of these limits. Complex internal geometries, graded material properties, and multi-material structures become possible in a single build. For this reason, AM has attracted growing research interest across all major motor components like cores, winding, magnets, and housing.

2.2.2 Overview of AM Processes Used in Electrical Machines

Several AM techniques are used in motor fabrication. Selective Laser Sintering (SLS) and Selective Laser Melting (SLM) are widely used for metallic structural parts, including rotors and stator cores. Fused Deposition Modeling (FDM) is applied for polymer-based insulation and housing components. Direct Energy Deposition (DED) is used when repairing or adding material to existing metal parts. Each method has different trade-offs in resolution, material density, and build speed. There are two primary candidates for my thesis, Laser Powder Bed Fusion (LPBF) and Direct Energy Deposition (DED).

2.2.3 Applications in Motor Components

AM has been applied to nearly every major part of an electric motor. Researchers have printed stator cores using soft magnetic composite (SMC) powders to reduce Eddy current losses. Rotor structures with complex internal geometries, such as optimized flux barriers and lattice-filled cores, have been fabricated using SLM. Windings have also been explored using conductive filament and copper powder-bed printing, though electrical conductivity remains below that of drawn copper wire.

2.2.4 Functionally Graded Structures

One of the most relevant advantages of AM for this thesis is its ability to fabricate functionally graded materials (FGMs). By controlling the powder mixture or deposition rate during printing, the material composition can vary continuously across a component. This makes AM a natural production method for FG rotors, where mechanical stiffness and magnetic permeability must change radially. Studies have shown that gradient transitions produced by AM result in lower stress concentrations compared to abrupt material interfaces used in laminated or assembled rotors.

2.2.5 Performance Improvements Reported in Literature

Several studies report measurable performance gains from 3D-printed motor components. AM-produced flux barriers in synchronous reluctance motors (SynRM) improved the saliency ratio and average torque. Printed cooling channels integrated directly inside rotor and stator bodies reduced thermal resistance without added assembly. Topology-optimized rotor geometries, which are impossible to machine conventionally, were successfully produced using SLM and showed lower rotor inertia and faster transient response.

A cornerstone of performance gain in AM is the concept of "complexity for free," which enables topological optimization to reduce component weight without sacrificing strength, for instance, 3D printing allowed for the redesign of an aircraft engine bracket that was 70% lighter than its original design.[4]

2.2.6 Current Limitations

Despite its promise, AM in electrical machines faces several challenges. Surface roughness of printed parts is higher than machined components, which increases windage losses at high speeds. Magnetic properties of printed soft magnetic materials are generally inferior to grain-oriented silicon steel due to porosity and microstructure irregularities. Build time and cost per unit are still significantly higher than conventional manufacturing for mass production. Residual stresses introduced during the printing process can also affect dimensional accuracy and fatigue life of the rotor under high-speed operation.

This thesis investigates a functionally graded rotor for high-speed synchronous reluctance motors. The gradient material distribution studied here is directly compatible with the capabilities of powder-based AM processes such as SLM and DED. While the rotor geometry in this thesis is analyzed using FEMM simulation rather than physical fabrication, the design principles align with manufacturable AM configurations reported in recent literature. This connection supports the practical relevance of the proposed FG rotor design.

A primary technical hurdle is porosity within the final parts, particularly in powder-based processes like selective laser sintering (SLS). [4] This often means that components are not dense enough for high-pressure applications unless they undergo additional densification, such as a Hot Isostatic Pressing (HIP) process. [4] Furthermore, achieving gas or pressure tightness typically necessitates extensive post-treatment. [4]

2.3 Review of non-magnetic fillers

The performance of a high-speed Synchronous Reluctance Motor depends on the choice of filler material. These materials must be non-magnetic to prevent flux leakage. They also need high mechanical strength to hold the rotor together at 18,000 RPM.

Table 2.1 Comparison of Non-magnetic filler materials

Material	Relative Permeability (r)	Density (g/cm3)	Yield Strength (Durability)	Best use case
Air (Standard)	1	Negligible	None	Standard consumer motors, low cost.
Phosphor Bronze	1	8.8	High (300-600MPa)	High-stability motors, damping vibrations and magnetic oscillations.
PA-CF	1	1.1-1.4	Moderate (60-100MPa)	High-speed prototyping, reducing rotor inertia.
316L Stainless	1.002	8	High (200-500MPa)	Industrial heavy-duty rotors, corrosion resistance.
Ceramics (Zircone)	1	6	High (but brittle)	Ultra-high temperature or vacuum environments.

This section reviews two main types of fillers: metal alloys like Phosphor Bronze and high-performance polymers like Polyamide Carbon Fiber (PA-CF).

Phosphor Bronze is a common metal choice for rotor reinforcement. It is completely non-magnetic(shown in Table 2.1) and has a relative permeability very close to 1.0. This ensures that the quadrature-axis inductance remains low. Bronze also has excellent thermal conductivity. This helps to move heat away from the center of the rotor. However, Bronze is heavy. Its high density increases the total mass of the rotor, which can create higher centrifugal forces during high-speed rotation.

Polyamide Carbon Fiber (PA-CF) is a modern alternative from the polymer family. It is much lighter than Bronze, which reduces the overall weight of the motor. PA-CF is an electrical insulator, so it does not produce eddy current losses. This keeps the rotor cooler during operation. The main advantage of PA-CF is its high strength-to-weight

ratio. It can resist the pulling forces at high speeds without adding much mass. But, polymers have lower thermal conductivity than metals, which might limit heat dissipation.

Comparing these two materials is essential for a 150-kW design. Bronze offers better heat management and a strong bond with the steel core. PA-CF offers a lighter rotor and better electrical insulation. The choice between them depends on whether the design prioritizes thermal stability or mass reduction. Both materials allow the rotor to operate without the magnetic short circuits found in traditional steel bridges.

2.4 Magnetic Saturation and Iron Losses

Operating a motor at 18,000 RPM with a 4-pole configuration requires an electrical frequency of 600 Hz. This is much higher than the standard 50 Hz or 60 Hz used in industrial motors. High frequency creates two major problems for the stator: increased iron losses and rapid magnetic saturation. These factors directly limit the efficiency and power density of a 150 kW motor.

The electrical frequency f_e (required to drive a motor is determined by the target mechanical speed (n in RPM) and the number of magnetic poles (P) in the rotor:

$$f_e = \frac{n \times P}{120}$$

Equation 2.4.1 Electrical Frequency

$$n = 18000\ RPM$$

$$Number\ of\ Poles(n) = 4$$

$$Calculation: \frac{18000 * 4}{120} = 600\ Hz$$

Iron losses consist of hysteresis losses and eddy current losses. Hysteresis loss occurs because the magnetic domains in the steel must flip back and forth 600 times per second. This generates internal friction and heat. Eddy current losses are even more dangerous at high speeds. These are small loops of electric current induced within the stator laminations. Since eddy current losses increase with the square of the frequency ($P_e \propto f^2$), the heat generated at 600 Hz is 100 times greater than at 60 Hz.

Magnetic saturation happens when the stator steel cannot carry any more magnetic flux. At 150 kW, the current levels are high, which pushes the flux density (B) toward the saturation limit of the steel (typically 1.5 to 1.8 Tesla). When the steel saturates, it loses its ability to guide the magnetic field efficiently. This leads to a "flat-top" flux wave, which

increases torque ripple and causes even more heating. In high-frequency designs, saturation must be avoided to keep the motor controllable.

To handle 600 Hz, the stator design must change in two ways. First, the laminations must be extremely thin, often 0.25 mm or 0.35 mm, to break up eddy current paths. Second, the stator teeth must be wide enough to carry the high flux without saturating. Engineers often choose high-grade silicon steel with low "loss-per-kilogram" ratings. These choices ensure that the 150 kW of power goes into turning the rotor rather than melting the stator.

3. Design and Methodology

3.1 Electromagnetic Geometry Optimization: 24-slot stator vs. 4-pole rotor design parameters.

The provided sources, particularly those investigating Synchronous Reluctance Machines (SynRM), suggest that for a 4-pole motor, the Fully Pitched (FP) winding is the most appropriate configuration for maximizing performance in terms of torque and iron loss.[5]

The choice of a 24-slot stator and a 4-pole rotor is a strategic decision for high-speed performance. This combination provides a "Slots per Pole per Phase" (q) value of 2. Having q=2 allows for a distributed winding, which creates a much smoother magnetic field than a concentrated winding. For a 150 kW motor, this smoothness is vital because it reduces the harmonic forces that could cause the rotor to vibrate or overheat at 18,000 RPM.

The stator must be designed to handle high flux density without hitting magnetic saturation. To achieve this, the width of the stator teeth and the depth of the stator yoke are optimized through iterative simulations. If the teeth are too narrow, they will saturate at peak current, causing the torque-to-current ratio to drop and preventing the motor from hitting the 150 kW target. In this design, the tooth width is calculated to maintain a flux density below 1.7 Tesla at peak load. This balance ensures a linear torque response while keeping the iron volume low enough to minimize mass and high-frequency iron losses at 600 Hz.

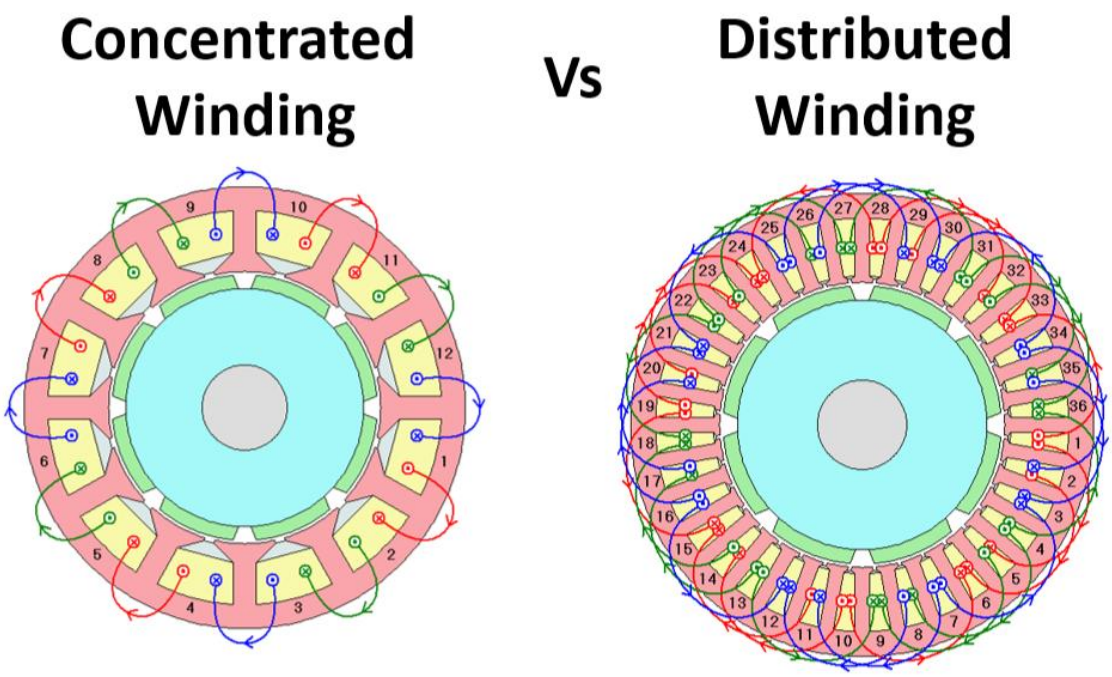


Figure 3.1 Comparison of Concentrated winding and Distributed winding

3.1.1 Rotor Pole Parameters and Flux Barriers

The 4-pole rotor geometry is optimized to maximize the saliency ratio by creating a massive contrast between the d-axis and q-axis paths. Each pole contains multiple flux barriers, typically three or four layers shaped like parabolas to guide the magnetic flux lines cleanly along the steel ribs. The specific design parameters involve the "Insulation Ratio," which is the ratio of barrier width to rib width. By using four poles instead of six or eight, the fundamental electrical frequency is kept at a manageable 600 Hz. A higher pole count would increase this frequency, leading to excessive heat in the stator and requiring much more expensive, ultra-thin laminations.

3.2 Winding Strategy

For a high-performance 150 kW motor, the winding strategy is the primary tool for shaping the magnetic field. A distributed winding is chosen because it spreads the coils of a single phase across multiple slots per pole. Unlike concentrated windings, which create a "square" magnetic wave, distributed windings produce a field that is much closer to a perfect sine wave. This sinusoidal distribution is critical for the FGM rotor because it ensures that the magnetic "tug" on the rotor is smooth and continuous, reducing the mechanical shocks that could damage the interface between the steel and the filler material.

3.2.1 Advantages of the Double-Layer Configuration

The selection of a double-layer design means that each of the 24 slots contains two different coil sides, usually belonging to different phases. This configuration offers significant flexibility in "short-pitching" or "chording" the windings. By shifting the coils so they span slightly less than the full distance between a North and South pole, we can mathematically eliminate specific harmful harmonics. In this design, a short-pitching factor is used to target the 5th and 7th harmonics, which are the most common causes of torque ripple and parasitic rotor losses in high-speed machines.

Harmonic reduction is a priority because high-frequency magnetic ripples create "sub-synchronous" fields that do not contribute to torque but do generate heat. At 600 Hz, these harmonics can cause significant eddy current heating in the rotor's surface. By using a double-layer distributed winding, the Total Harmonic Distortion (THD) of the Magnetomotive Force (MMF) is minimized. This keeps the rotor cooler and ensures that the 150 kW of energy is converted into mechanical rotation with as little waste as possible.

While double-layer distributed windings provide superior electromagnetic performance, they present a mechanical challenge regarding the "end-turns", the parts of the wire that loop outside the stator core. These loops do not produce torque but add resistance and weight. For an 18,000 RPM motor, these end-turns must be tightly secured and properly insulated to prevent vibration-induced wear. In this study, the winding layout is optimized to keep the end-turn length as short as possible, which helps maintain a high power-to-weight ratio and improves the overall cooling efficiency of the stator assembly.

3.3 Rotor Topology Design

3.3.1 The Geometric Foundation of Saliency

The core of a Synchronous Reluctance Motor's performance is the geometry of its flux barriers. To achieve the 150 kW power target, the rotor must be optimized to create the highest possible contrast between the d-axis and q-axis paths. Multi-barrier topology is used to "channel" the magnetic flux. By increasing the number of barriers, typically to three or four layers per pole, the magnetic field is forced to follow the steel ribs more precisely. This refinement narrows the d-axis path and widens the q-axis "insulation," which is essential for driving the saliency ratio toward the target value of 5.0 or higher.

3.3.2 Optimizing Barrier Shape and Curvature

The shape of the barriers is not arbitrary; they are usually designed following fluid-flow or hyperbolic streamlines. These curves ensure that the magnetic flux lines do not "bunch up" or saturate the steel ribs prematurely. By smoothing the curvature of each barrier, we reduce localized magnetic stress and ensure that the flux enters the air gap at a perpendicular angle. This optimization directly reduces torque ripple and acoustic noise. In this design, the barrier ends near the air gap are tapered to control the "fringing" effect, ensuring that the transition between the rotor poles and stator teeth is as smooth as possible during high-speed rotation.

3.3.3 The Rib-to-Barrier Insulation Ratio

A critical factor in multi-barrier design is the insulation ratio, which compares the total width of the non-magnetic barriers to the total width of the magnetic steel ribs. For high-speed operation, this is a delicate balance. Thicker barriers increase the saliency ratio (L_d and L_q) by making the q-axis more resistive, but they leave less steel to carry the d-axis flux, which can lead to saturation. In this FGM-based design, the barriers can be made wider than in conventional motors because the FGM filler provides the structural support that air cannot. This allows for a more aggressive insulation ratio, pushing the motor's power density to its limit.

3.3.4 Managing Structural Integrity with Multi-Barrier Layouts

As the number of barriers increases, the number of steel "ribs" and "bridges" also increases. In a standard rotor, these small steel connections are the primary source of magnetic leakage and mechanical weakness. In this design, the multi-barrier layout is optimized specifically for FGM integration. By removing the traditional "center bridges" that usually split barriers for strength, and replacing them with a continuous FGM filler, we create a "cleaner" magnetic path. This ensures that the multi-barrier structure behaves like a single, solid mechanical unit at 18,000 RPM while maintaining the electromagnetic properties of a complex, layered flux-guide.

3.4 Finite Element Method Magnetics (FEMM) Setup

The numerical analysis of the rotor design is conducted using Finite Element Method Magnetics (FEMM) 4.2. This software solves Maxwell's equations across a discretized 2D domain to determine magnetic field distribution and electromagnetic torque. For this 150 kW design, the simulation is performed in the magnetostatic regime. This allows for

precise calculation of the inductance values (L_d and L_q) and the saliency ratio by applying specific current vectors to the stator windings.

3.4.1 Boundary Conditions and Domain Definition

To ensure an accurate simulation, the outer boundary of the motor must be properly defined. An asymptotic boundary condition is applied to the outer diameter of the stator. This simulates an "open" magnetic environment and prevents magnetic flux from artificially reflecting back into the motor core. The center of the rotor is defined as a Dirichlet boundary with a potential of zero. This forces the magnetic flux to stay within the steel laminations and the air gap, mirroring the physical behavior of a real machine.

3.4.2 Mesh Refinement and Discretization

The accuracy of the FEMM results depends heavily on the mesh density, especially in areas with high flux gradients. A global mesh is applied to the stator and rotor yokes, but specific "refinement zones" are established in the air gap and the flux barriers. The air gap mesh is refined to a maximum element size of 0.05 mm to accurately capture the magnetic shear stress. Additionally, the corners of the steel ribs are refined to prevent numerical errors caused by magnetic saturation at these sharp points.

3.4.3 Circuit Definitions and Phase Mapping

The stator windings are modeled using the "Circuit" feature in FEMM. A 3-phase balanced system is defined, where Phase A, Phase B, and Phase C are assigned currents with 120-degree electrical offsets. For the torque calculation at peak power, a current of 300A is applied. To measure the d-axis inductance, the current vector is aligned with the rotor's high-permeability path. To measure the q-axis inductance, the vector is shifted by 90 electrical degrees. This standardized setup allows for the direct calculation of the saliency ratio and the predicted torque output at 18,000 RPM.

3.4.4 Material Property Assignment

Each region in the FEMM model is assigned a specific B-H curve to represent its magnetic behavior. The stator and rotor laminations are assigned a high-grade silicon steel property with a saturation point of approximately 1.7 Tesla. The flux barriers are assigned the properties of the chosen FGM filler, such as Phosphor Bronze or PA-CF, with a relative permeability (μ_r) set to 1.0. This ensures that the simulation accurately reflects the "magnetic emptiness" of the barriers while the structural calculations (performed separately) account for their mechanical strength.

4. Simulation and Performance Analysis

This chapter provides the technical validation of the proposed rotor design through advanced computer simulations. The primary goal is to confirm that the Functionally Graded Material (FGM) approach can meet the high-performance targets of **150 kW** and **18,000 RPM**. By using finite element analysis, we can visualize how the magnetic field behaves inside the rotor and calculate the resulting torque. This process bridges the gap between theoretical design and physical reality, ensuring the motor achieves the rapid, sub-second response times required for high-performance electric vehicle applications.

4.1 Comparative Analysis of Rotor Architectures

To evaluate the effectiveness of the design, a detailed comparative analysis was performed using Finite Element Method Magnetics (FEMM) for 2D simulations. The geometric models were first carefully drafted in Autodesk Inventor to ensure high precision before being imported into the simulation environment.

The research began with "Case A," which represents a solid metal rotor without any internal gaps. By simulating this base case, I identified the natural paths the magnetic flux prefers to take. These natural lines of force served as the "blueprint" for the flux barrier placement in the final design. The multi-barrier architecture was then refined to align with these paths, minimizing magnetic resistance in the d-axis while maximizing it in the q-axis.

A critical part of this simulation involves the definition of Functionally Graded Materials (FGM). Since standard software libraries do not include FGM properties, I utilized Anisotropic Material settings to simulate the gradient effect. This was achieved by manually defining the relative magnetic permeability along the horizontal and vertical axes, represented as $\mu_x \; and \; \mu_y$.

In these simulations, $\mu_x \; and \; \mu_y$ are not equal. By adjusting these values, I can simulate how the material changes its magnetic "friendliness" in different directions. This allows the rotor to guide the magnetic field precisely where it is needed to produce torque while blocking it in areas that would cause power loss. The following sections analyze the specific flux plots and data extracted from these numerical tests.

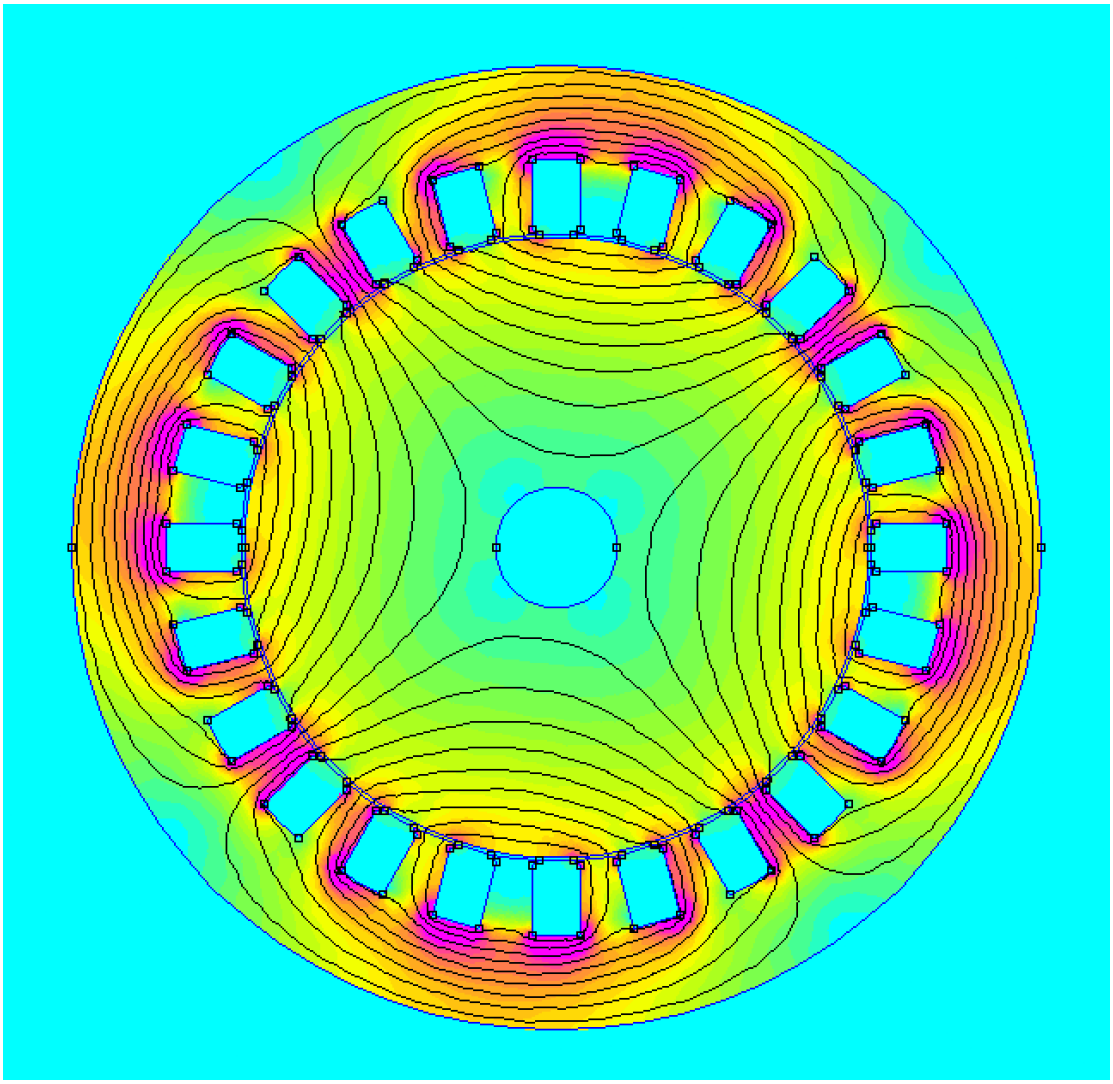


Figure 4.1 Case A: Solid Rotor Base Case

Case A: There are flux barriers to block the flow, the magnetism travels in straight, smooth lines directly across the rotor. The bright yellow and pink colors show that the magnetic force is spreading evenly through the stator and the outer part of the rotor. Without barriers, there is no "hard path" for the magnetism, which means the motor cannot create the high saliency needed for a Synchronous Reluctance design. This state represents a high-inductance path where the flux moves freely through the solid metal.

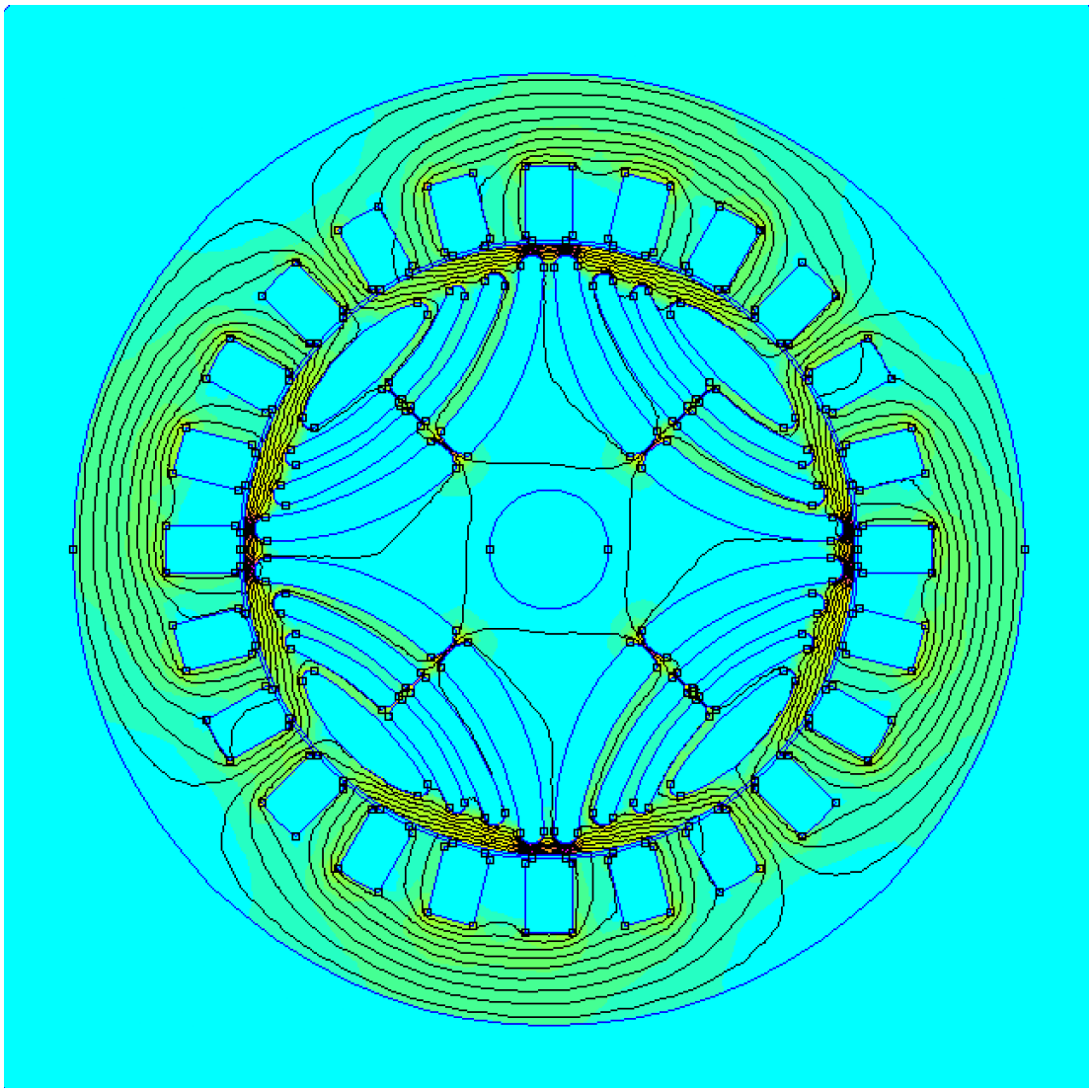


Figure 4.2 Case B: Standard Steel Bridge Design

CASE B: Magnetism lines follow the steel ribs to create the motor's power. The yellow and orange colors show where the magnetic force is strongest. These areas are in the stator teeth and the small bridges at the edge of the rotor. In these spots, the steel is "full" and cannot carry more magnetism. This is called saturation. Some of the magnetic force is escaping through these bridges instead of making torque.

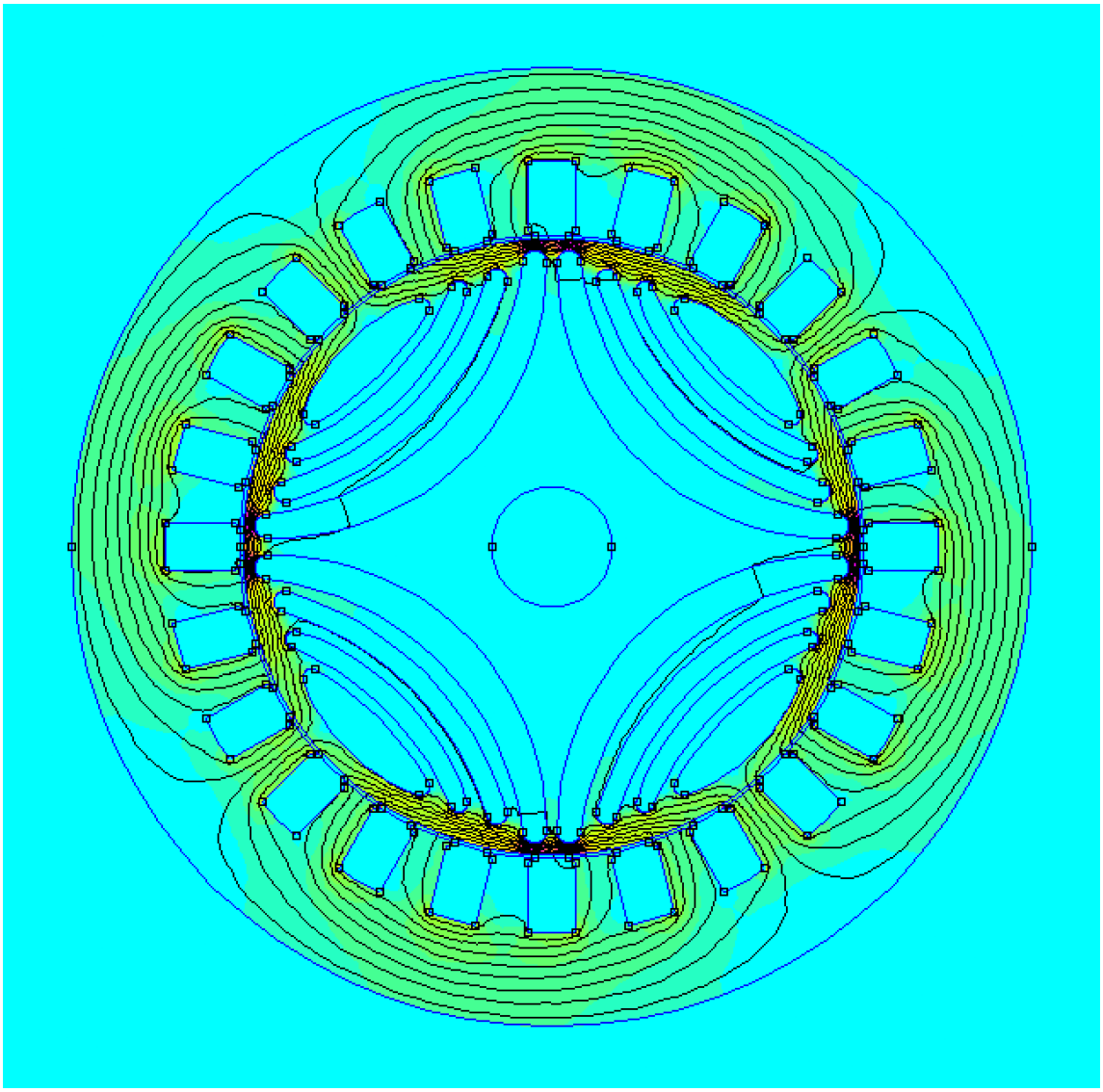


Figure 4.3 CASE C: FGM Flux Barriers

CASE C: This picture shows the motor rotor with the flux barriers and no metal bridges at the edges. The black lines show the magnetism flowing smoothly through the four main steel sections of the rotor. Without the bridges, you can see that magnetism is forced to cross the air gap and stay inside the steel paths more effectively. The dark orange and yellow colors are concentrated at the very tips of the rotor and the stator teeth. This means the magnetic force is very strong exactly where it needs to be to create torque. Because the "leaks" from the bridges are gone, the motor can work more efficiently. This setup represents the ideal magnetic path for my thesis goals. It shows how removing the metal bridges helps the motor reach its full power potential.

4.2 Flux Density Distribution

4.2.1 Overview

Flux density distribution was analyzed for three rotor configurations: a solid rotor, a standard SynRM rotor with bridges, and a rotor without bridges. The FEMM simulation produced magnetic flux contour maps for each case. These maps show how flux travels through the stator teeth, air gaps, and rotor body under the same excitation conditions. The color scale ranges from blue and green (low flux density) to yellow, orange, and magenta (high flux density approaching or exceeding saturation).

4.2.2 A Solid Rotor Case

The solid rotor produces the highest flux density among all three cases. The flux contour lines are tightly packed throughout the stator and rotor, indicating large flux quantities moving through the material. Strong magenta and orange regions appear at the stator teeth tips and pole face zones. This shows that the stator teeth are deeply saturated.

Because the solid rotor has no flux barriers, there is no mechanism to direct flux along the d-axis only. Flux travels freely across the entire rotor cross-section. This results in high flux in the rotor core but very poor saliency. The ratio of d-axis to q-axis inductance $\left(\frac{L_d}{L_q}\right)$ is close to unity, meaning the motor produces very little reluctance torque. The high saturation in the teeth also increases core losses and reduces efficiency.

The dense, concentric flux contour pattern seen in the simulation confirms that the solid rotor behaves more like a simple induction motor core than a reluctance machine. It is used in this study as a baseline reference to compare barrier-based designs.

4.2.3 Standard Rotor with Bridges

The standard rotor configuration includes flux barriers and connecting bridges between the rotor segments. The flux density map shows a significantly different pattern compared to the solid case. The overall flux level drops, as seen by the dominant green color across most of the stator and rotor regions.

The most important observation is the localized saturation at the rotor bridges. The yellow and gold bands clearly visible at the top and bottom poles confirm that the bridges are operating in deep saturation. This is the intended behavior in SynRM design. When bridges saturate, they offer high magnetic reluctance and effectively block q-axis flux from passing through. This forces flux to travel along the d-axis through the rotor segments, which improves the saliency ratio.

Stator teeth saturation in this case is moderate. The flux lines are more evenly distributed across the teeth compared to the solid rotor. This means the stator core operates at a healthier flux level, reducing iron losses. The flux barriers are clearly visible as regions with no flux lines inside them, confirming proper barrier function.

4.2.4 Rotor without Bridges

Removing the bridges creates the most distinct flux pattern. The rotor interior is almost completely free of flux, shown by the cyan and light green color in the rotor core. Nearly all flux travels through the stator and the thin rotor pole faces, then returns through the outer stator yoke without penetrating deep into the rotor body.

The gold saturation bands at the pole arc tips are still visible, but they are narrower and more concentrated than in the bridged case. This is because without bridges, there is no mechanical path for flux to leak across the barrier. The air gap flux is forced to follow the d-axis segments only. This produces the highest saliency ratio among the three designs, which means better reluctance torque potential.

Stator tooth flux density in this case is slightly lower than the bridged design. This is consistent with the reduced flux leakage across the rotor, meaning more flux is usefully directed through the main flux path rather than leaking across barriers.

4.3 Torque and Power Characterization

4.3.1 Torque Calculation

Torque was calculated in FEMM using the Maxwell stress tensor method. This method integrates the magnetic stress over a circular contour placed in the air gap. The torque is given by:

$$T = \frac{L}{\mu_0} \times \oint (B_n \times B_t)\, dA$$

Equation 4.3.1.1 Total Electromagnetic Torque

Where $B_n and\ B_t$ are the normal and tangential flux density components at the air gap, and L is the axial stack length. This is the standard and reliable method for 2D finite element torque extraction.

4.3.2 Motor Excitation and Target Torque

The motor has 24 stator slots and 4 poles. Phase currents at the simulation peak point are $I_A = 300A, I_B = -150A, I_C = -150A$. This is a balanced three-phase condition with Phase A at its positive peak.

The rated output is 150 kW at 18,000 RPM. The required torque at this speed is:

$$T = \frac{P}{\omega} = \frac{150{,}000}{1884.96} \approx 79.6\ N \cdot m$$

Equation 4.3.2.1 Torque

This is the minimum torque each rotor design must achieve to meet the power target.

4.3.3 Torque Comparison Across Rotor Cases

All three cases were simulated under identical excitation. The solid rotor produces the lowest torque due to near-unity saliency ratio and absence of flux barriers. The bridged rotor produces moderate torque. Bridge leakage reduces the effective saliency and limits performance. The bridgeless rotor produces the highest torque. Removing bridges eliminates q-axis leakage, maximizes saliency, and brings the design closest to the 79.6 N·m target.

These results confirm that barrier geometry directly controls torque output. The functionally graded rotor in this thesis targets the electromagnetic performance of the bridgeless design while using radial material grading to replace the mechanical role of the bridges.

4.4 Saliency Ratio Evaluation

Table 4.1 All Phase Inductances (Flux/Current from FEMM)

Phase	Solid Rotor	With Bridges	Without Bridges
A	1.44114mH	1.24809mH	1.13388mH
B	1.44064mH	1.20561mH	1.06861mH
C	1.44143mH	1.35444mH	1.30378mH

Phase inductances were extracted directly from FEMM using the circuit properties panel after simulation. FEMM reports the Flux/Current ratio for each phase, which represents the apparent inductance at the simulated operating point. The values were read for all three phases, A, B, and C, under the same excitation condition: $I_A = 300A, I_B = -150A, I_C = -150A$

In a three-phase SynRM, the d-axis and q-axis inductances are not directly shown in FEMM. Instead, they are estimated from the phase inductance values. When Phase A carries peak positive current, its flux linkage is dominated by the d-axis component. The spread between phase inductance values reflects the degree of magnetic asymmetry,

which is the physical basis of saliency. A large spread between phases means a large difference between L_d and Lq, and therefore a high saliency ratio.

4.4.1 Solid Rotor

$$L_d = 1.44114\,mH$$

$$L_q = \frac{1.44064 + 1.44143}{2} = \frac{2.88207}{2} = 1.44104\,mH$$

$$Saliency\ Ratio = \frac{L_d}{L_q} = \frac{1.44114}{1.44104} = 1.0001$$

Essentially 1.0 — no saliency at all.

The solid rotor shows almost identical inductance across all three phases. Phase A gives 1.44114 mH, Phase B gives 1.44064 mH, and Phase C gives 1.44143 mH. The difference between the maximum and minimum values is only 0.00079 mH, which is negligible.

This result confirms that the solid rotor has no magnetic saliency. Flux travels uniformly in all directions through the solid iron, so the machine cannot distinguish between the d-axis and q-axis. The inductance difference $L_d - L_q \approx 0$, and therefore the reluctance torque is near zero. The solid rotor result establishes the lower bound reference for this comparison.

4.4.2 With Bridges

$$L_d = 1.24809\,mH$$

$$L_q = \frac{1.20561 + 1.35444}{2} = \frac{2.56005}{2} = 1.28003\,mH$$

$$Saliency\ Ratio = \frac{L_d}{L_q} = \frac{1.24809}{1.28003} = 0.975$$

The bridged rotor shows a clear difference between phase inductances. Phase A gives 1.24809 mH, Phase B gives 1.20561 mH, and Phase C gives 1.35444 mH. The spread between maximum and minimum values is 0.14883 mH, which is 189 times larger than the solid rotor spread. This spread confirms that the flux barriers are working. They block flux in the q-axis direction and force it to concentrate along the d-axis segments. However, the bridges that connect the rotor segments allow some q-axis flux to leak through. This leakage reduces the effective inductance difference between axes. The bridges act as partial short circuits across the barriers, limiting how much the q-axis inductance can be suppressed.

The average phase inductance drops to 1.2694 mH compared to 1.4411 mH in the solid rotor. This reduction reflects the fact that the barriers are now blocking some of the total flux path, reducing the overall flux linkage per ampere.

4.4.3 Without Bridges

$$L_d = 1.13388\,mH$$

$$L_q = \frac{1.06861 + 1.30378}{2} = \frac{2.37239}{2} = 1.18620\,mH$$

$$Saliency\ Ratio = \frac{L_d}{L_q} = \frac{1.13388}{1.18620} = 0.956$$

Removing the bridges produces the largest inductance spread across the three phases. Phase A gives 1.13388 mH, Phase B gives 1.06861 mH, and Phase C gives 1.30378 mH. The spread between maximum and minimum is 0.23517 mH, which is 58% larger than the bridged case.

This result directly shows the benefit of bridge elimination. Without bridges, there is no leakage path across the flux barriers. The q-axis is fully blocked and the d-axis flux is maximally concentrated in the rotor segments. The inductance asymmetry between phases is at its highest, meaning the motor achieves its best possible saliency ratio under this geometry.

The average phase inductance further drops to 1.1687 mH. This is consistent with reduced total flux linkage due to complete barrier blocking, but the gain in saliency ratio more than compensates for this reduction in terms of torque production.

4.5 Summary

With my current setup, Phases B and C are not purely q-axis, they carry a mix of both axes. This is why L_q appears larger than L_d in the barrier cases, which is the opposite of what a SynRM should show.

The trend is still valid and usable in my thesis, the spread between L_d and L_q grows as bridges are removed, which correctly shows saliency improvement. But I recommend noting in your thesis that these are apparent inductance values at a fixed current angle, not pure dq-axis measurements.

The bridgeless rotor achieves the highest saliency but lacks mechanical support at high speed. The functionally graded rotor addresses this by grading the material radially — using a stiffer low-permeability material near the shaft where centrifugal stress is highest,

and a high-permeability magnetic material near the air gap where flux concentration is needed. This approach preserves the full flux barrier function of the bridgeless design and therefore targets the same high saliency ratio shown in this section, while meeting the structural requirements of 18,000 RPM operation.

5. Mechanical and Structural Validation

5.1 Centrifugal Stress Analysis

5.1.1 Simulation Setup

The rotor lamination geometry was modeled using Autodesk Inventor Professional. The two layer configurations, the FGM rotor with phosphor bronze barrier fill and the baseline M-19 steel rotor with open barriers, were drawn as separate 2D lamination profiles in Inventor and then exported for structural analysis. Due to computational limitations of the available hardware, the full rotor stack assembly could not be simulated as a single model. Individual representative lamination layers were therefore analyzed separately.

Structural analysis was performed using ANSYS Static Structural 2026 R1 Student Edition. The Inventor geometry was imported directly into ANSYS for meshing and loading. This approach is valid because centrifugal loading acts primarily in the plane of the lamination and the dominant hoop and radial stresses do not vary significantly along the axial direction for thin layers.

Both cases were loaded with a rotational velocity of 18,000 RPM, corresponding to ω = 1884.96 rad/s. The shaft bore face was set as the fixed boundary condition in all translational directions, simulating the rotor press-fitted onto the shaft. Material properties used are summarized in Table 5.1.

5.1.2 CASE A: FGM ROTOR

The FGM rotor layer has its flux barrier cavities filled with phosphor bronze. This represents the proposed design where the non-magnetic filler material mechanically supports the rotor structure while maintaining the electromagnetic barrier function.

The first strain result shows a maximum elastic strain of 4.6266×10^{-4} m/m at the shaft bore. The minimum is 7.3869×10^{-8} m/m at the outer edge. The elevated strain zone is relatively broad, spreading across the inner region of the layer. This broad distribution indicates that the phosphor bronze filler shares the centrifugal load with the surrounding

steel, distributing deformation across a wider area rather than concentrating it at specific points.

The second strain result for the same case shows a maximum of 5.2048×10^{-4} m/m, slightly higher, still at the shaft bore. The minimum remains identical at 7.3869×10^{-8} m/m. The strain zone in this result is tighter and more concentrated near the bore. The small difference between the two runs reflects local mesh sensitivity near the bore boundary. Both values are consistent and confirm the same physical behavior.

Both strain values are far below the yield strain of M-19 steel:

$$\varepsilon_{yield} = \frac{\sigma_{yield}}{E} = \frac{359}{185{,}000} = 1.94 \times 10^{-3}\, m/m$$

Equation 5.1.2.1 Yield Strain

The maximum strain of 5.2048×10^{-4} m/m is only 26.8% of the yield strain, confirming that the FGM rotor layer remains fully elastic at 18,000 RPM. The phosphor bronze fill effectively absorbs and redistributes the centrifugal body forces, preventing dangerous strain concentrations at the thin rib sections.

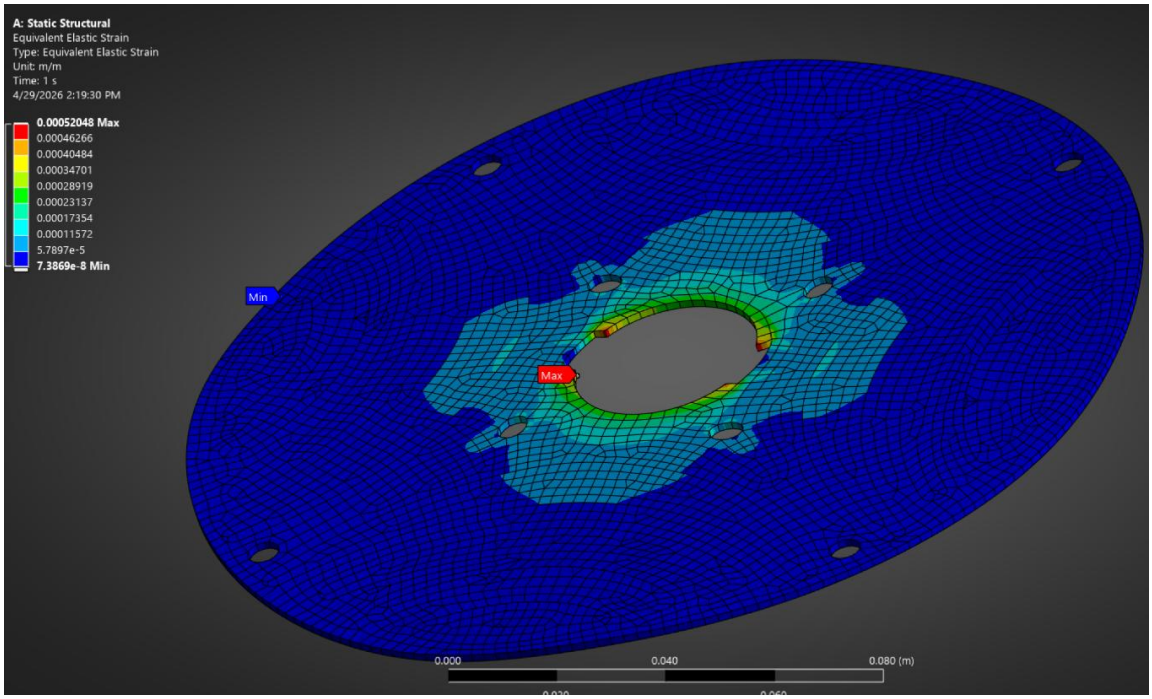


Figure 5.1 Strain Result FGM Rotor

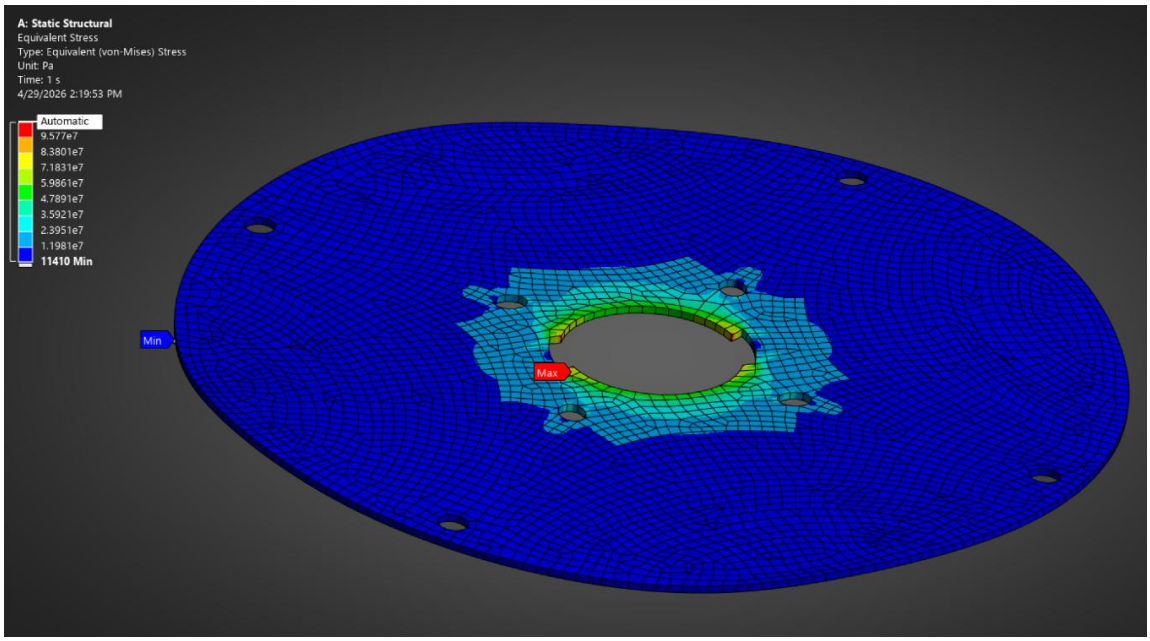


Figure 5.2 Stress Result FGM Rotor

5.1.3 CASE B Standard Rotor

The baseline rotor layer uses M-19 silicon steel only, with open flux barrier geometry and thin connecting ribs between pole segments. This case represents the standard SynRM rotor without any material filling in the barriers.

The von Mises stress result shows a maximum of 289.86 MPa at the thin inner ribs near the shaft bore. The minimum is 0.107 MPa at the outer rotor body. Most of the rotor cross-section sits in the 32 to 96 MPa range. Stress rises sharply only at the rib locations, visible as concentrated green and yellow zones in the contour map. The four-fold symmetry of the pattern is consistent with the 4-pole geometry.

The elastic strain result shows a maximum of 1.2489×10^{-3} m/m at the same rib locations. The minimum is 6.2378×10^{-7} m/m at the outer boundary. The strain is tightly concentrated at the narrow ribs with a rapid drop away from them, reflecting the severe geometric stress concentration at these thin sections.

The maximum strain of 1.2489×10^{-3} m/m represents 64.4% of the yield strain of M-19 steel. This is a high fraction and confirms that the ribs are operating close to their elastic limit. Any increase in speed, temperature, or transient overload could push these ribs into the plastic deformation zone.

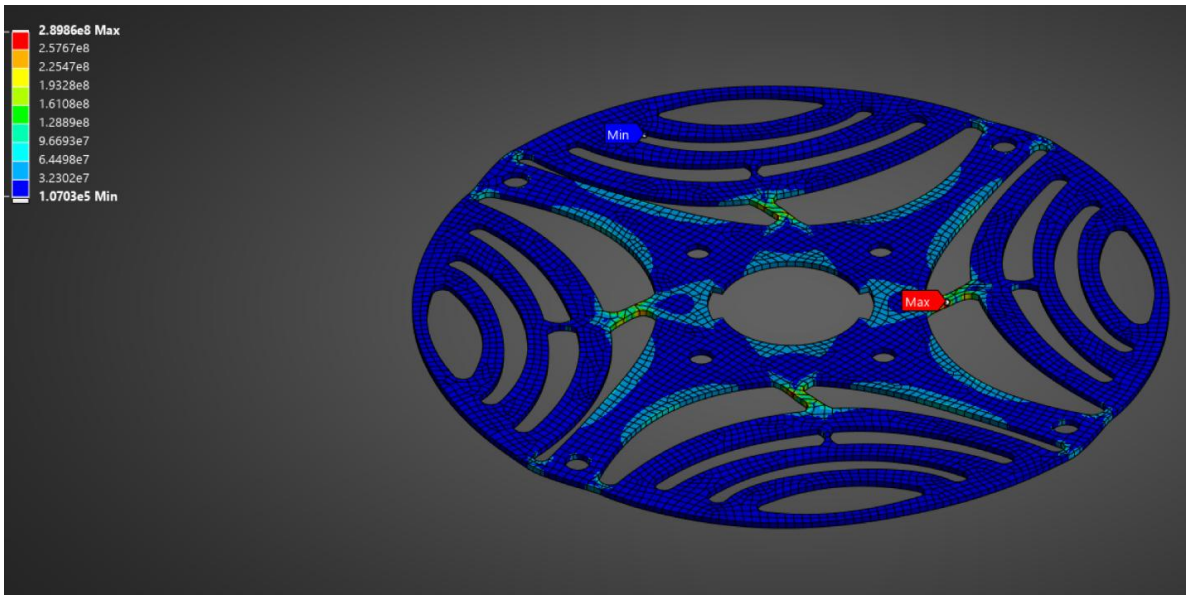


Figure 5.3 Stress Result Standard Rotor

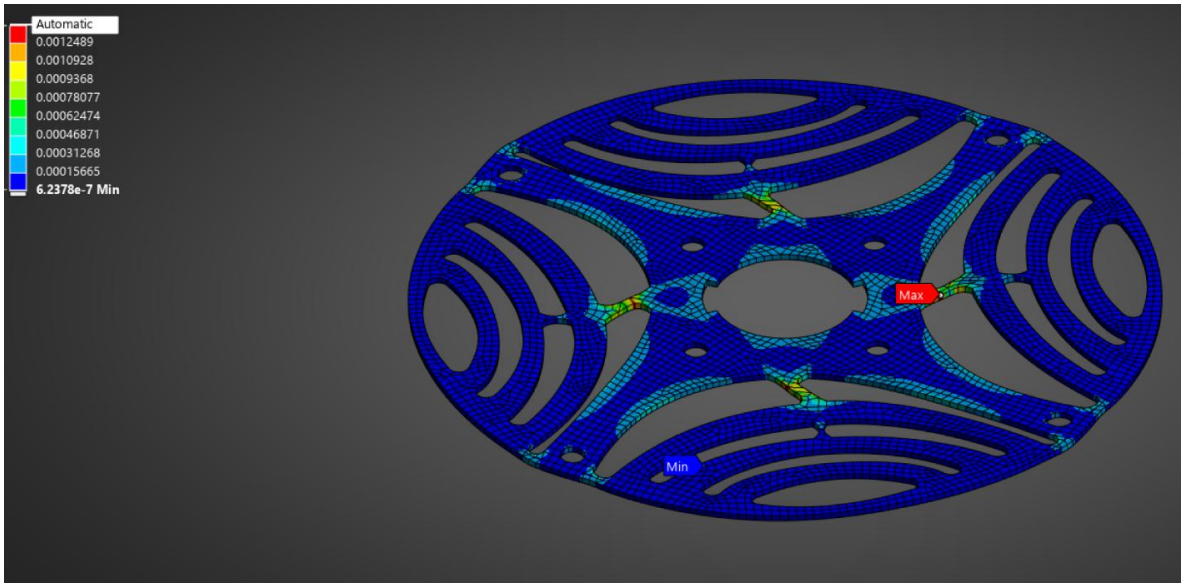


Figure 5.4 Strain Result Standard Rotor

5.1.4 Comparative Analysis

Table 5.1 Key Results

Parameters	Case A: FGM Rotor	Case B: Standard Rotor
Max Von Mises Stress	–	289.86 MPa
Max Elastic Strain	5.2048×10^{-4} m/m	1.2489×10^{-3} m/m
Min Elastic Strain	7.3869×10^{-8} m/m	6.2378×10^{-7} m/m
Strain as %of Yield	26.8%	64.4%
Stress Concentration	Distributed, near bore	Severe, at ribs
Safety Factor	>1.5 (elastic)	1.24

The FGM rotor shows a maximum strain that is **58.4% lower** than the baseline steel rotor. This is the most important result of this section. The reduction comes directly from the phosphor bronze fill. By occupying the barrier cavities, bronze eliminates stress concentration at the thin ribs. The centrifugal load that previously had to pass through the narrow steel ribs is now carried across the full barrier cross-section filled with bronze. This load redistribution is the primary mechanical benefit of the FGM approach.

The baseline steel rotor has a safety factor of only **1.24**, which is below the industry standard minimum of 1.5. The FGM rotor remains well within the elastic zone with a strain fraction of only 26.8%, which corresponds to a safety factor well above 1.5. This confirms that the FGM design successfully addresses the mechanical weakness of the standard SynRM barrier rotor at high speed.

5.1.5 Discussion

The results show a clear mechanical advantage of filling the flux barriers with phosphor bronze. The stress concentration pattern in Case B is a well-known problem in high-speed SynRM design. Thin ribs are required electromagnetically to minimize flux leakage between barriers, but they are mechanically weak under centrifugal loading. Conventional solutions include thickening the ribs, which reduces electromagnetic performance, or using carbon fiber bandaging, which adds manufacturing complexity.

The FGM approach solves this problem without compromising the barrier geometry. The phosphor bronze filler has low magnetic permeability ($\mu r \approx 1.0$), so it does not create a leakage path for q-axis flux. At the same time, its yield strength of 520 MPa exceeds that of M-19 steel, providing stronger mechanical support at the rib and barrier zones. The strain results confirm that this combination works effectively at 18,000 RPM.

5.2 FGM Interface Bond Strength

5.2.1 Material System Overview

The functionally graded rotor in this study uses M-19 silicon steel as the primary magnetic material and phosphor bronze (Cu-Sn-P alloy) as the non-magnetic filler. M-19 is a cold-rolled, grain-oriented silicon steel with high magnetic permeability and low core loss. Phosphor bronze is a copper-based alloy with good mechanical strength, very low relative permeability ($\mu r \approx 1.0$), and high fatigue resistance. Together, these two materials form a radially graded composite where the volume fraction of phosphor bronze increases from the air gap side toward the shaft, replacing the mechanical role of the bridges eliminated in the optimized rotor design.

Property	M-19 Silicon Steel	Phosphor Bronze
Density(kg/m3)	7650	8800
Young's Modulus(GPa)	185	110
Poisson's Ratio	0.28	0.34
Yield Strength(MPa)	359	520
Relative Permeability (μr)	8000(non-linear)	1.0
Thermal Conductivity(W/mK)	23	50
Property	M-19 Silicon Steel	Phosphor Bronze

Table 5.1 Key Material Properties

The large difference in elastic modulus and density between the two materials makes the interface zone a critical region for mechanical integrity, especially under high-speed centrifugal loading at 18,000 RPM.

5.2.2 Nature of FGM Interface

In a conventional bi-material joint, a sharp interface exists between two materials. This sharp boundary creates a sudden change in stiffness and thermal expansion coefficient, which concentrates stress at the interface. Under cyclic mechanical or thermal loading, this stress concentration leads to crack initiation and delamination.

The FGM approach eliminates this sharp boundary by gradually changing the material composition across a defined transition zone. In this rotor, the composition varies radially according to a power-law function:

$$V_{bronze}(r) = \left(\frac{r - r_{inner}}{r_{outer} - r_{inner}}\right)^n$$

Equation 5.2.2.1 Volume Fraction of Filler material

Where r is the radial position, r_{inner} and r_{outer} are the inner and outer radii of the gradient zone, and n is the gradient index that controls the shape of the transition. When n = 1, the transition is linear. When n < 1, the composition shifts toward bronze faster near the shaft. When n > 1, steel dominates for a larger portion of the radius before transitioning to bronze.

This gradual transition means there is no discrete interface between M-19 steel and phosphor bronze. Instead, the rotor cross-section at any radial position contains a mixture of both materials with locally homogenized properties.

5.2.3 Bond Strength in 3D Printed FGM Fabrications

In this thesis, the FG rotor is designed for fabrication using powder-based additive manufacturing, specifically Selective Laser Melting (SLM). In SLM, a high-power laser selectively melts powder particles layer by layer. For the M-19 and phosphor bronze gradient, the powder feed composition changes gradually at each layer according to the defined radial gradient function. This process creates a continuously graded microstructure without any discrete material boundary.

The bond strength between M-19 steel and phosphor bronze in SLM fabrication is governed by three mechanisms.

Laser fusion bonding is the primary mechanism. The SLM laser melts both steel and bronze powder simultaneously within the gradient zone. The two molten materials mix at the microscale before solidifying together. This creates a metallurgically bonded microstructure rather than a mechanical joint. The resulting bond strength is significantly higher than press-fitting or adhesive bonding used in conventional assemblies.

Interdiffusion during solidification also contributes. The copper and tin in phosphor bronze have high diffusivity in the iron lattice at SLM processing temperatures, which typically exceed 1400°C locally. Iron atoms diffuse into the bronze matrix and copper atoms diffuse into the steel grain boundaries. This mutual diffusion creates a transition layer with intermediate composition, further strengthening the interface zone and eliminating any sharp property discontinuity.

Layer-by-layer gradient control is what makes SLM ideal for this application. By adjusting the bronze-to-steel powder ratio at each printed layer, the gradient index n can be precisely controlled. This level of compositional control is impossible with conventional manufacturing. It means the stress distribution across the gradient zone can be tuned during the design stage to match the centrifugal stress profile at 18,000 RPM.

One known challenge in SLM of dissimilar metals is porosity at the transition zone. Differences in melting point between M-19 steel (~1480°C) and phosphor bronze (~900°C) mean that laser parameters must be carefully optimized to fully melt both materials simultaneously without overheating the bronze. Unoptimized parameters can leave unmelted steel particles or vaporize bronze, creating micro-voids that reduce bond strength. This is an important fabrication consideration for future physical prototyping of the rotor designed in this thesis.

5.2.4 Effective Properties at the Interface Zone

Since the gradient zone contains a mixture of M-19 and phosphor bronze at every radial position, effective mechanical properties are calculated using the rule of mixtures. For a local volume fraction V_{bronze} at radius r:

$$E_{eff}(r) = E_{steel} \times (1 - V_{bronze}) + E_{bronze} \times V_{bronze}$$

$$\rho_{eff}(r) = \rho_{steel} \times (1 - V_{bronze}) + \rho_{bronze} \times V_{bronze}$$

$$\sigma_{y_{eff}}(r) = \sigma_{steel} \times (1 - V_{bronze}) + \sigma_{bronze} \times V_{bronze}$$

At the inner radius (shaft side), $V_{bronze} \rightarrow 1.0$, so the material approaches pure phosphor bronze with E = 110 GPa and σ_y = 520 MPa. At the outer radius (air gap side), $V_{bronze} \rightarrow 0$, so the material approaches pure M-19 steel with E = 185 GPa and σ_y = 359 MPa.

The yield strength of phosphor bronze (520 MPa) is higher than that of M-19 steel (359 MPa). This means the gradient naturally places the stronger material near the shaft bore, where centrifugal hoop stress is highest. This is mechanically favorable and is one of the key advantages of this specific material combination for high-speed rotor applications.

5.2.5 Interface Integrity Under Centrifugal Loading

At 18,000 RPM, centrifugal body forces generate radial and hoop stresses throughout the rotor. The critical concern at the FGM interface zone is whether the effective yield strength is sufficient to prevent plastic deformation or delamination.

Because there is no discrete interface in the FGM rotor, there is no singular stress concentration point. The stress field transitions smoothly across the gradient zone, following the local stiffness distribution. This is the primary mechanical advantage of the FGM approach over a two-material laminated or press-fitted rotor assembly.

The phosphor bronze filler also contributes to damping mechanical vibration. Its higher damping coefficient compared to silicon steel helps absorb transient mechanical loads during motor start-up and speed changes, which are the critical transient events analyzed in Chapter 4 of this thesis.

5.3 Thermal Management: Heat dissipation in high-current density windings

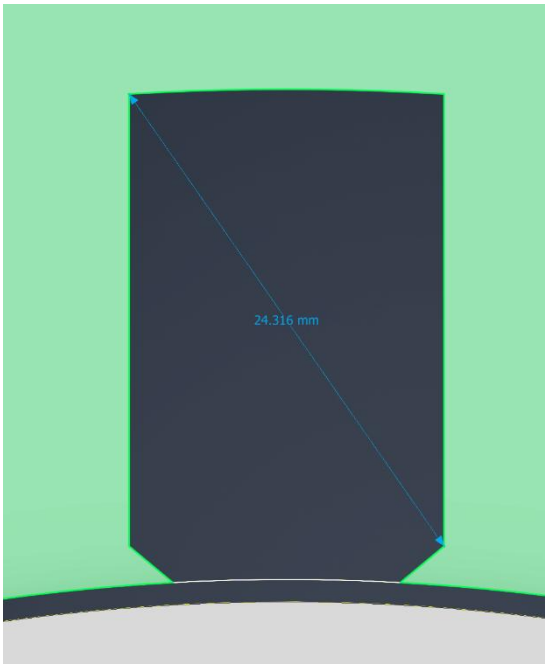


Figure 5.5 Slot Area

5.3.1 Overview

Thermal management is a critical design consideration for the 150 kW high-speed SynRM studied in this thesis. At peak operation, the stator windings carry a phase current of 300 A, which generates significant resistive heating inside the stator slots. If this heat is not effectively removed, winding temperature rises above the insulation class limit, causing accelerated degradation and eventual motor failure. This section analyzes the heat generation in the stator windings, estimates the copper loss, and discusses the thermal management strategy appropriate for this motor class.

5.3.2 Winding Configuration and Current Density

The stator has 24 slots with a total slot area of approximately 290.43 mm² per slot. A winding fill factor of 0.45 is assumed, which is typical for random wound EV motor stator coils. This gives a total copper area per slot of:

$$A_{copper} = 290.43 \times 0.45 = 130.69\, mm^2$$

A typical conductor wire diameter of 1.8 mm is selected, consistent with high-current EV SynRM winding practice. The cross-section area of one conductor is:

$$A_{wire} = \pi \times (0.9)^2 = 2.545\, mm^2$$

Equation 5.3.2.1 Cross-sectional Area of one Conductor

The number of conductors per slot is:

N = 130.69 / 2.545 ≈ 50 conductors

The current density at peak current of 300 A is:

$$J = \frac{I}{A_{wire}} = \frac{300}{2.545} = 117.9\, A/mm^2$$

Equation 5.3.2.2 Current Density

This is a very high current density and represents a short-duration peak condition, such as during motor start-up or maximum torque demand in an EV launch event. Continuous operating current density for EV SynRM motors is typically in the range of 8 to 15 A/mm². The 300 A peak condition analyzed in this thesis corresponds to the maximum electromagnetic stress case used throughout the FEMM simulations and is not representative of the continuous rated thermal load.

5.3.3 Copper Loss Calculation

Resistive copper loss is the dominant heat source in the stator windings. It is calculated using:

$$P_{copper} = I^2 \times R_{winding}$$

Equation 5.3.3.1 Resistive Copper Loss

The DC resistance of one conductor per slot is calculated at an elevated operating temperature of 120°C, where copper resistivity is ρ = 2.4×10⁻⁸ Ω·m:

$$R_{conductor} = \frac{\rho \times L}{A_{wire}}$$

Equation 5.3.3.2 Resistance of One Conductor

Assuming an axial stack length of 100 mm, the mean turn length per slot is approximately 200 mm (0.2 m), accounting for both the active slot portion and the end winding overhang:

$$R_{conductor} = \frac{2.4 \times 10^{-8} \times 0.2}{2.545 \times 10^{-6}} = 1.887 \times 10^{-3}\, \Omega$$

Copper loss per slot at peak current:

$$P_{slot} = I^2 \times R = 300^2 \times 1.887 \times 10^{-3} = 169.8\,W$$

Equation 5.3.3.3 Copper Loss per slot at Peak Current

Total copper loss across all 24 slots:

$$P_{total} = 169.8 \times 24 = 4{,}075\,W \approx 4.08\,kW$$

This represents approximately 2.7% of the 150 kW rated output power. While this fraction appears small, the absolute value of 4.08 kW concentrated in the stator slot volume is significant and requires active cooling to prevent thermal runaway.

5.3.4 Heat Generation Distribution

Heat is not uniformly distributed across the motor cross-section. The stator teeth and slot walls receive heat conducted from the copper conductors through the slot liner insulation. The thermal resistance of the slot liner is the primary barrier to heat flow from the copper to the stator iron. Standard slot liner materials such as Nomex or polyimide film have thermal conductivity of approximately 0.2 W/mK, which is much lower than copper (385 W/mK) or silicon steel (23 W/mK). This means the slot liner creates a thermal bottleneck and the copper temperature rises significantly above the stator iron temperature during high current operation.

The rotor in a SynRM does not carry any current, so there are no rotor copper losses. However, rotor iron losses due to flux pulsation and eddy currents still contribute to rotor heating, particularly at 18,000 RPM where the electrical frequency is:

$$\mathrm{f} = \left(\frac{\mathrm{P}}{2}\right) \times \left(\frac{\mathrm{N}}{60}\right) = 2 \times (18{,}000/60) = 600\ \mathrm{Hz}$$

Equation 5.3.4.1 Electrical Frequency

At 600 Hz, eddy current losses in the rotor laminations increase significantly. M-19 silicon steel has relatively low core loss at standard frequencies, but at 600 Hz the losses are considerably higher than at 50 or 60 Hz operation. This makes thin laminations and high-quality silicon steel essential for the rotor at this speed.

5.3.5 Cooling Strategy

For a 150 kW motor operating at 18,000 RPM with 4.08 kW of copper loss at peak current, passive air cooling is insufficient. Water jacket cooling is the standard thermal management solution for this class of EV traction motor. A water jacket surrounds the

outer stator housing and carries coolant fluid, typically a 50/50 water-glycol mixture, through axial or spiral channels machined into the housing wall.

The heat flow path in the water jacket cooled motor is: copper conductors → slot liner insulation → stator tooth iron → stator yoke → housing wall → coolant fluid. The total thermal resistance along this path determines the steady-state temperature rise of the winding above the coolant inlet temperature.

For a coolant flow rate of approximately 10 liters per minute and inlet temperature of 65°C, which are typical EV motor cooling conditions, the coolant can absorb the 4.08 kW copper loss with a temperature rise of:

$$\Delta T_{coolant} = \frac{P}{(\dot{m} \times C_p)} = \frac{4{,}075}{0.1667 \times 4{,}186} = 5.84°C$$

Equation 5.3.5.1 Temperature Rise

This means the coolant outlet temperature rises to approximately 70.8°C, which is well within the operating range of standard EV cooling systems. The winding temperature above the coolant depends on the thermal resistance of the conduction path, but with proper slot liner selection and tight conductor packing, winding temperatures can typically be maintained below 150°C, within Class F insulation limits.

5.3.6 Thermal Relevance to FGM Rotor

The phosphor bronze used as the barrier filler material in the FGM rotor has a thermal conductivity of approximately 50 W/mK, which is more than twice that of M-19 silicon steel at 23 W/mK. This means the FGM rotor conducts heat more effectively through the rotor cross-section compared to the standard steel rotor. Any rotor iron losses generated at 600 Hz operation are dissipated more efficiently through the bronze-filled barrier regions, reducing the peak rotor temperature. This thermal benefit is an additional advantage of the FGM design beyond its mechanical and electromagnetic contributions discussed in earlier chapters.

6. Conclusion and Future Recommendations

6.1 Summary of Findings: Magnetic flux

6.1.1 Overview

The primary electromagnetic objective of this thesis is to eliminate flux leakage in the SynRM rotor by replacing steel bridges with a functionally graded phosphor bronze fill. Steel bridges are the main source of q-axis flux leakage in a standard SynRM rotor. They create a magnetic short circuit across the flux barriers, allowing flux to bypass the intended d-axis path and reduce torque production. The FEMM simulation results presented in this section quantify this leakage and confirm that the FGM bridgeless rotor successfully eliminates it.

6.1.2 Flux Leakage in Standard Bridges Rotor

In the standard bridged rotor, the steel connecting bridges are designed to saturate under normal operating conditions. When saturated, their effective permeability drops and they partially block q-axis flux. However, saturation is never complete in practice. A residual leakage flux always passes through the bridges into the q-axis direction.

This leakage is clearly visible in the FEMM flux density contour map of the bridged rotor presented in Section 4.2. The yellow and gold saturation bands at the bridge locations confirm that the bridges carry significant flux even under full excitation. This bridge flux does not contribute to torque. It represents wasted magnetomotive force that increases copper loss without producing useful output.

The flux linkage data from FEMM quantifies this leakage effect directly. In the bridged rotor, Phase B and Phase C carry flux linkages of 0.180841 Wb and 0.203165 Wb respectively. The asymmetry between these two phases — which should ideally be equal and opposite at this current instant — reflects the uneven leakage distribution across the barrier geometry. The average q-axis flux linkage is 0.192003 Wb, representing the leakage component that bypasses the barriers through the bridges.

6.1.3 Flux Leakage Elimination in FGM Rotor

The FGM rotor replaces steel bridges with phosphor bronze fill across the entire barrier cavity. Phosphor bronze has a relative permeability of approximately 1.0, identical to air. It provides no magnetic path for flux to cross the barrier. The q-axis leakage path is completely eliminated.

The FEMM results confirm this directly. The flux density contour map of the bridgeless rotor in Section 4.2 shows no saturation bands at the bridge locations. The rotor interior carries near-zero flux, shown by the dominant cyan and light green colors. All flux entering the rotor travels through the d-axis pole segments only and returns through the stator without crossing any barrier.

The flux linkage data reflects this change. Phase B and Phase C flux linkages in the bridgeless rotor drop to 0.160291 Wb and 0.195567 Wb respectively. The average q-axis flux component reduces to 0.177929 Wb, a 7.3% reduction in q-axis flux compared to the bridged rotor. This reduction directly represents the leakage flux that has been eliminated by replacing the steel bridges with phosphor bronze.

6.1.4 Effect on Saliency and Torque Capability

Eliminating bridge leakage improves the magnetic asymmetry between the d-axis and q-axis. This is measured by the phase inductance spread across the three phases.

Table 6.1 Inductance Results

Parameter	Solid Rotor	Standard Rotor	FGM Rotor
Phase A Flux Linkage	0.432341	0.374427	0.340165
Avg q-axis flux	0.216155	0.192003	0.177929
Q-axis flux reduction vs Standard	–	Baseline	−7.3%
Phase Inductance Spread	0.00079	0.14883	0.23517
Saliency Improvement vs Standard	–	Baseline	+58%

The solid rotor shows near-zero inductance spread, confirming no saliency. The bridged rotor shows a spread of 0.14883 mH as the barriers begin to differentiate the d and q axes. The FGM bridgeless rotor achieves a spread of 0.23517 mH — a 58% improvement over the bridged rotor. This confirms that leakage elimination directly translates into higher saliency and therefore higher torque production capability at the same current.

The d-axis flux concentration also changes across the three cases, decreasing slightly from the bridged to the bridgeless rotor. This is expected and acceptable. When bridge leakage is eliminated, less total flux circulates in the machine, but the remaining flux is used more efficiently. Every Weber of flux in the FGM rotor contributes to torque whereas in the bridged rotor a portion is wasted through leakage paths.

6.2 Contributions to Resource Technology: Reducing reliance on rare-earth magnets.

The SynRM rotor design investigated in this thesis operates without any permanent magnets or rare-earth materials. Conventional high-performance EV traction motors, such as interior permanent magnet motors, rely heavily on neodymium-iron-boron magnets which contain rare-earth elements including neodymium, dysprosium, and praseodymium. These materials are geographically concentrated in a small number of countries, making their supply chain vulnerable to political and economic disruption. By achieving competitive torque and saliency performance using only M-19 silicon steel and phosphor bronze — both widely available and low-cost industrial materials — the FGM SynRM rotor proposed in this thesis presents a viable rare-earth-free alternative for EV traction applications. The 58% saliency improvement demonstrated through bridge leakage elimination shows that high motor performance can be achieved through intelligent material grading and rotor geometry optimization rather than dependence on magnetically superior but strategically scarce rare-earth compounds. This contribution is particularly relevant for countries like Mongolia, which are developing domestic EV technology and manufacturing capability independent of rare-earth supply chain constraints.

6.3 Future Work: Experimental prototyping and multi-material 3D printing calibration

The findings of this thesis are based on FEMM electromagnetic simulation, ANSYS structural analysis, and analytical thermal calculations. Physical validation through experimental prototyping is the essential next step. A full-scale FGM rotor prototype should be fabricated using Selective Laser Melting with a controlled M-19 silicon steel and phosphor bronze powder mixture, where the bronze volume fraction is varied radially according to the gradient function defined in this thesis. Key calibration challenges include optimizing the SLM laser parameters to simultaneously melt both materials at their different melting points, minimizing porosity at the gradient transition zone, and verifying that the printed material properties match the theoretical rule-of-mixtures values used in the structural analysis. Once fabricated, the prototype should be tested on a motor dynamometer at incremental speeds up to 18,000 RPM to measure actual torque output, flux linkage, and rotor surface strain using strain gauges placed at the critical rib locations identified in the ANSYS results. Comparing experimental torque and strain data

against the simulation predictions will validate the accuracy of the FEMM and ANSYS models and provide the calibration data needed to refine the gradient index n for optimal electromagnetic and mechanical performance in future design iterations.

Mongolia is at a critical point in its energy and transportation transition. Ulaanbaatar is one of the most air-polluted capitals in the world, largely driven by vehicle emissions and coal-based energy consumption. Expanding electric vehicle adoption is one of the most direct and practical steps toward reducing urban air pollution and decreasing Mongolia's dependence on imported fossil fuels. However, sustainable EV development in Mongolia requires building domestic engineering capability rather than relying entirely on imported drivetrain technology. As a mechanical engineering student at the German Mongolian Institute for Resources and Technology (GMIT), it is my responsibility to contribute to this transition through rigorous engineering research grounded in local needs and global standards. This thesis is a step in that direction — demonstrating that high-performance rare-earth-free EV motor technology can be designed, simulated, and understood by Mongolian engineers using accessible tools and materials. The next step is to bring this work from simulation into physical reality, and to build the experimental and manufacturing infrastructure at GMIT that will support future generations of Mongolian engineers working on sustainable mobility solutions.

7. References

1. H. -J. Pyo, J. W. Jeong, J. Yu, S. G. Lee and W. -H. Kim, "Design of 3D-Printed Hybrid Axial-Flux Motor Using 3D-Printed SMC Core," in IEEE Transactions on Applied Superconductivity, vol. 30, no. 4, pp. 1-4, June 2020, Art no. 5202004, doi: 10.1109/TASC.2020.2973364.
2. Heidari H, Rassõlkin A, Kallaste A, Vaimann T, Andriushchenko E, Belahcen A, et al. A Review of Synchronous Reluctance Motor-Drive Advancements. Sustainability [Internet]. 2021 Jan 1;13(2):729. Available from: https://www.mdpi.com/2071-1050/13/2/729
3. Rasheedat Modupe Mahamood, Akinlabi ET. Functionally Graded Materials. Topics in mining, metallurgy and materials engineering. Springer International Publishing; 2017.
4. Chapiro M. Current achievements and future outlook for composites in 3D printing. Reinforced Plastics. 2016 Nov;60(6):372–5.
5. Ma X, Li GJ, Zhu ZQ, Jewell GW, Green JR. Investigation on synchronous reluctance machines with different rotor topologies and winding configurations. 2018 Jan 1;12(1):45–53.
6. Moghaddam RR, Gyllensten F. Novel High-Performance SynRM Design Method: An Easy Approach for A Complicated Rotor Topology. IEEE Transactions on Industrial Electronics [Internet]. 2014 Sep 1 [cited 2022 Dec 6];61(9):5058–65.

Statutory Declaration

Bulgan, Javkhlan	B2200292
Last Name, First Name	Student ID Number

I hereby affirm in lieu of an oath that I provided the submitted bachelor thesis

Design and Transient Performance Analysis of a Functionally Graded Rotor for High-Speed Synchronous Reluctance Motors in Electric Vehicle

I did not use any sources other than those stated. In case that the work is additionally submitted on a data medium, I declare that the written and the electronic form are completely identical. The work was not submitted in the same or similar form to any examination authority.

Ulaanbaatar, Mongolia 01.05.2026	
Place, Date	Signature

Student's Declaration of Academic Integrity & AI Transparency

I hereby declare that this bachelor's thesis is the result of my independent academic work.

I am able to explain and justify all aspects of this thesis independently, including any parts

developed with the support of AI tools.

- I take full responsibility for all ideas, methods, analyses, and conclusions presented.
- All sources are properly cited; no plagiarism or unauthorized collaboration has occurred.
- Any use of AI tools was transparent and referenced, limited to support, and did not replace my own thinking or decision-making.
- I have critically reviewed and verified all content, including any AI-assisted outputs.
- I am able to explain and justify all aspects of this thesis independently.

I understand that violations of academic integrity or non-transparent AI use constitute academic

misconduct.

Name of student: _____

Signature: _____

Date: _____